Iraqi Geological Journal

Journal homepage: https://www.igj-iraq.org

Neo-Tethyan Tectonic Evolution: Implications from Petrogenesis of Mafic Rocks in the Bulfat Complex, Zagros Suture Zone, Northeast of Iraq

Randi G. Shabo[1*] and Ahmed M. Aqrawi[1]

[1] Department of Earth Science and Petroleum, College of Science, Salahaddin University, Erbil, Iraq

[*] **Correspondence:** randi.shabo@su.edu.krd

Received:
17 October 2025
Accepted:
9 January 2026
Published:
31 March 2026

Abstract

The Bulfat Complex in the Penjween-Walash Subzone of the Zagros Suture Zone, northeast of Iraq, comprises mafic, granitoid, and ultrabasic rocks over an area of 100 km². This study investigates the petrogenesis and tectonic setting of mafic rocks from the Kela suite, located northeast of Darshmana village in the Qala Diza area, through petrography, mineral chemistry, and geochemistry. The studied mafic rocks of the Bulfat Complex predominantly consist of plagioclase, pyroxene, and olivine minerals and are classified as gabbro, olivine gabbro, and troctolite. Those rocks display a wide range of igneous textures, including granular, ophitic, sub-ophitic, poikilitic, corona, porphyroclastic, exsolution, and mesh textures. Mineral chemistry Electron Probe Micro Analyses analyses show plagioclase (bytownite–labradorite), diopside clinopyroxene, chrysolite olivine, and secondary calcic amphibole, mainly pargasite. Whole-rock ICP-MS analysis reveals high SiO_2, MgO, Al_2O_3, Fe_2O_3, CaO, and low alkalis and TiO_2 with calc-alkaline to subalkaline affinity. The REE patterns show enrichment in LREEs (La/Sm)n=1.43, compared to HREEs. The enrichment in LILE (Sr and Ba) and depletion in HFSEs (Nb and P) indicate an island arc environment. Tectonic discrimination diagrams, together with negative Nb-Zr anomalies and positive Sr-Ba-K anomalies further support formations in subduction-related arc setting. Whole-rock geochemical data, Fe-Mg enrichment, and trace element characteristics suggest fractional crystallization from mantle-derived magmas. Geothermobarometry yields crystallization temperatures of 750-1016˚C (average 890˚C) and a pressure of 5-10 kbar (average 6.5 kbar), corresponding to an emplacement depth of 19-21 km under a warm subduction zone. These conditions reveal a low-angle subduction of old Neo-Tethyan (Albian-Cenomanian) and a slow convergence rate (< 2 cm/ year), yielding an estimated total convergence distance of the Neo-Tethyan Ocean to be around 324 km during Paleogene subduction.

Keywords: Mafic rocks; Bulfat Complex; Zagros Suture Zone; Neo-Tethyan Ocean; Petrogenesis; Northeast of Iraq

1. Introduction

The Bulfat Complex, encompassing the study area, is situated within the Iraqi Zagros Suture Zone (Fig. 1A), a region formed by the closure of the Neo-Tethys Ocean and the subsequent collision between the Arabian and Eurasian plates (Alavi, 1994; Agard et al., 2005). The Bulfat Complex consists of a wide variety of igneous rock types and forms a predominant section of the Upper Allochthon (the ophiolite-bearing terrain) and contains a volcano-sedimentary unit known as the Gemo-Qandil Group (Jassim et al., 2006). This group was initially referred to as the Bulfat Group (Jassim et al., 1982).

The Bulfat Complex covers an area of 100 km^2, comprises mafic and ultramafic igneous rocks, and is intruded by several minor dykes (Jassim et al., 1982; Jassim and Buday, 2006; Aswad et al., 2013). The Complex is mainly composed of old and young intrusions (Buda, 1993; Sofy and Aqrawi, 2007). The older intrusion primarily includes pyroxene-hornblende and gabbro-diorites, and a younger intrusion of olivine gabbro-diorites is accompanied by syenite and nepheline syenite resulting from late-stage magmatic differentiation (Jassim et al., 2006; Aswad et al., 2016; Zrary et al., 2022). The mafic rocks of the Bulfat Complex are a key component in understanding the geological history and multi-stage tectonic evolution of the Neo-Tethys Ocean in the Zagros Suture Zone

Recent studies include Zrary (2019), who investigated the petrogenesis and geochemistry of gabbroic rocks of the Bulfat Complex at Shakha Rash Mountain, NE Iraq. Al-Hamed et al. (2020) examined the dioritic-gabbroic pegmatites in the Bulfat Complex, NE Iraq. Although several earlier studies have examined the mafic rocks of the Bulfat Complex, a detailed investigation of the Kela location that focuses on petrography, mineral chemistry, and geochemistry remains limited.

Field investigations revealed that mafic rocks make up a large area of the Bulfat Complex and include several types, such as troctolite, olivine gabbro, gabbro, and pyroxene hornblende gabbro. They are in contact with thermal metamorphic rocks, like marble and display various igneous structures, including rhythmic layering and enclave structures (Zrary, 2019)

The study area is located in the northeast of Iraq, specifically 65 km north of Sulaimaniya city and 20 km east of Qala Diza town; between latitudes (36° 11′ 2.8104–36° 11′ 1.9824) and Longitudes (45° 18′ 46.148–45° 18′ 38.977) (Fig. 1B). Road access to the study area was restricted due to security concerns, which required permission approval to cross the Iraqi checkpoint at the Iraq-Iran border. Geologically, the study area is located within the Bulfat Complex of the Zagros Suture Zone, within the Penjween-Walash Subzone (Buday and Jassim, 1987). The rock samples were collected from Kela suite that is located 5.5 km east of Darshmana village and 20 km east of Qala Diza town.

This study focuses on mafic rocks of the Bulfat Complex by investigating their petrography, mineral chemistry and geochemical characteristics, with the aim of revealing their petrogenesis and tectonic setting during emplacement. This study involves understanding how regional tectonic events such as subduction, collision, and rifting affected the formation of these mafic rocks in the Bulfat Complex by linking their petrogenesis with these events.

2. Geological Setting

The Zagros orogenic belt is located in the central Alpine-Himalayan orogenic system. This orogenic belt is estimated to be around 2000 km long with a NW-SE trend, stretching from southern Europe, Middle East, and southwest Asia (Alavi, 1994; Agard et al., 2005; Azizi and Moineraziri, 2009; Moghadam and Stern, 2015; Moghadam et al., 2019). The Zagros orogenic belt was formed by the collision between the Arabian and Eurasian plates due to the consumption of the Neo-Tethys Ocean (Alavi, 1994; Agard et al., 2005). Numerous magmatic activities occurred along the Zagros Orogenic Belt that led to the formation of various ophiolite complexes. The Iraqi Zagros ophiolites from southeast to the northwest are Penjween, Mawat, Bulfat, Pushtashan, and Hasanbag (Ali et al., 2019).

The Zagros orogenic belt consists of four parallel tectonic zones (Urmieh-Dokhtar Magmatic Arc, Sanandaj-Sirjan Zone, Zagros Fold-Thrust Belt (ZFB), and Mesopotamian Foreland Basin) (Alavi, 1994). The ZFB is characterised by two thrust sheets formed in the Neo-Tethys. The Lower Allochthonous, known as the Walash-Naopurdan nappe, consists of volcano-sedimentary rocks. The Upper Allochthonous, known as ophiolite-bearing terranes, including Bulfat, Mawat, and Penjween Complexes (Aswad, 1999), are probably of Albian-Cenomanian age (97-105 Ma) (Ali et al., 2019).

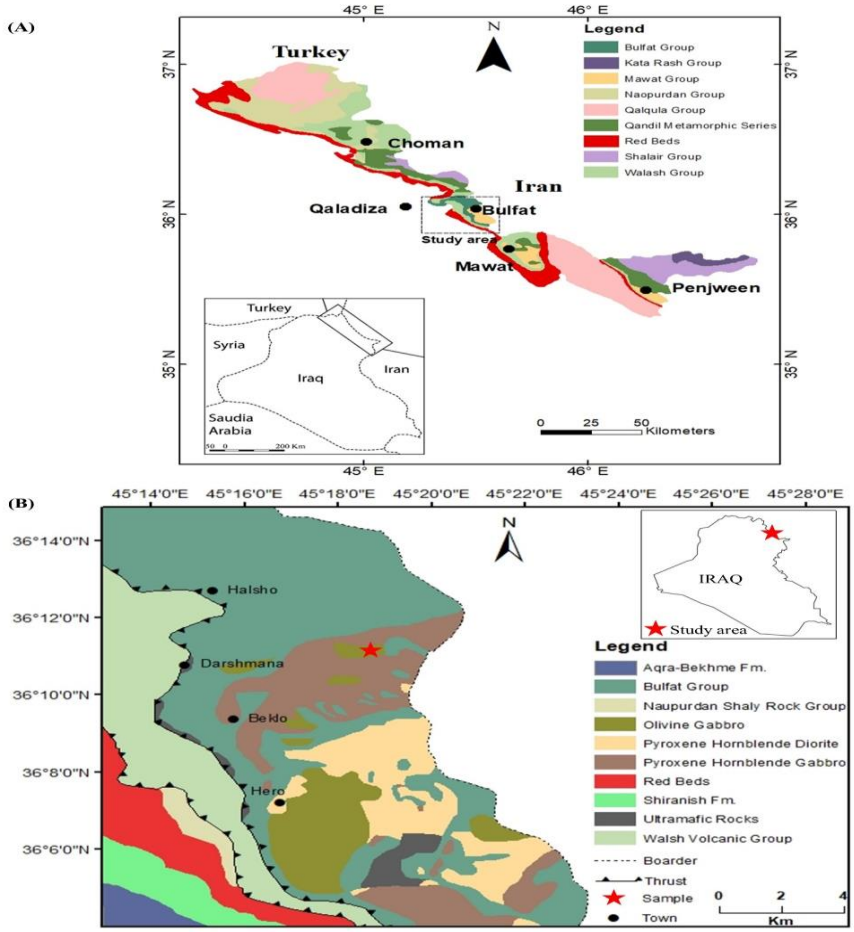

Fig.1. A) Geological map of Zagros Suture Zone after Sissakian and Fouad, 2015; B) Geological map of the Bulfat igneous intrusion showing the locations of the studied mafic samples (modified from Buda, 1993)

These two sheets were thrust over the Arabian Plate margin during two separate phases of subduction and collision in the Late Cretaceous to Miocene (Jassim and Buday, 2006).

The Bulfat Complex is a part of the Iraqi Zagros Suture Zone and consists of the volcano-sedimentary sequence of the Gimo-Qandil Group (Jassim et al., 2006), which was initially referred to as the Bulfat Group (Jassim et al., 1982). The Bulfat Group has been affected by two stages of intrusion; an older intrusion primarily includes pyroxene-hornblende and gabbro-diorites, and a younger intrusion of olivine gabbro-diorites (Jassim et al., 2006). Additionally, it consists of syenite and nepheline syenite formed during the late stage of magmatic differentiation (Jassim et al., 2006; Aswad et al., 2016). The Bulfat Complex is composed of acidic, intermediate, mafic, ultramafic, and pegmatitic rocks, which appear as dikes and massive bodies of varying thicknesses, as well as metasedimentary rocks that occur as xenoliths (Al-Hamed et al., 2019; Zrary et al., 2022). The mafic rocks, the focus of this research, form a large area of the Bulfat Complex and are typically observed in the field as large, massive bodies associated with other ultramafic rocks (Fig. 2A). The blocky and massive outcrops indicate the rock's high resistance to weathering (Winter, 2014). On fresh surfaces, mafic rocks are dark gray to black (Fig. 2B), whereas altered and weathered surfaces exhibit yellow to dark brown hues (Fig. 2C). Common alteration minerals include serpentine, chlorite, and sericite. The essential minerals, like plagioclase and

pyroxene, are identifiable to the naked eye. Plagioclase typically appears as white or light gray crystals, while pyroxene is dark, sometimes displaying greenish or brownish shades.

3. Analytical Methods

For this proposed study, a field investigation was conducted to collect 50 samples of mafic rocks from the Kela suite. A total of 30 thin sections were prepared and examined using polarized microscopes at the laboratory of the Geology Department, University of Salahaddin, to identify mineralogy and textures. A point counter method was used to determine the modal mineral percentages.

Mineral chemistry was determined at Charles University in Prague, Czech Republic, with Electron Probe Micro Analyses (EPMA) technique using a FEG-EPMA JXA-8530F (Jeol) microprobe under operating conditions of 15 kV accelerating potential and 20 nA beam current, and the ZAF online program was used for data correction.

Whole-rock geochemical analyses, encompassing major, trace, and rare earth elements, as well as loss-on-ignition, were conducted at ALS Laboratory Group in Seville, Spain. Thirteen samples were chosen for whole-rock geochemical analyses. Major oxides were determined by inductively coupled plasma-atomic emission spectrometry (ICP-AES) following lithium borate fusion (ME-ICP-06), with additional determinations of total major elements obtained using a total fusion ICP-AES method (TOT-ICP06). Trace and rare earth elements were analyzed by inductively coupled plasma-mass spectrometry (ICP-MS) after lithium borate fusion (ME-MS81), whereas selected trace elements were determined using a four-acid digestion procedure (ME-4ACD81). Loss on ignition (LOI) values were measured by gravimetric analysis (OA-GRA05).



Fig.2. Photographs of the studied mafic rocks of the Bulfat Complex: A) Huge mafic rocks in the studied location; B) Fresh dark grey surface of the mafic rocks; C) Weathered layers of the mafic rocks

4. Results

4.1. Petrographic Characteristics

The modal mineral percentages of the studied mafic rocks were obtained through the point counting method (Table 1). Following recalculation into the Pl–Px–Ol mineral system, the data were plotted on the Pl–Px–Ol ternary diagram (Fig. 3). According to Streckeisen (1974 and 1976), the studied mafic rocks are classified as gabbro, olivine gabbro, and troctolite (Fig. 3)

4.1.1. Olivine gabbro

The most common rock type in the study area is dark grey in color, with a mineral composition of plagioclase (45-73%), clinopyroxene (6-31%), and olivine (5-24%), along with minor orthopyroxene (0-1%), amphibole (0-5%), and opaque minerals (1-7%). Secondary minerals include chlorite and serpentine. The rock exhibits a medium- to coarse-grained, granular interlocking texture (Fig. 4A). Plagioclase grains (0.5-4 mm) are subhedral to anhedral, lath-like, and display orthocumulate texture with polysynthetic twinning (Fig. 4B). Deformation is indicated by bent twins (Fig. 4B). Extinction of plagioclase angles ranges from 35° to 40°. Olivine (1-4 mm) is granular, irregular, and highly fractured. Olivine is often altered at the margins to fine-grained serpentine due to hydrothermal processes, with the presence of minor secondary Fe-oxides (Fig. 4C). Clinopyroxene (1-3 mm) is subhedral to anhedral, prismatic, and shows intercumulus texture. Amphibole occurs as rims around olivine and clinopyroxene, forming a corona texture. Accessory minerals such as pentlandite, pyrrhotite, chalcopyrite, rare sphalerite, and rare phlogopite were also observed in some samples (<1%) (Fig. 5A). The rock displays various textures, including poikilitic (Fig. 4A), where large oikocrysts enclose smaller chadocrysts, ophitic and subophitic (Fig. 4B), where pyroxene encloses plagioclase, and porphyroclastic texture (Fig. 4D), where large porphyroclasts are set in a finer-grained plagioclase matrix due to tectonic forces.

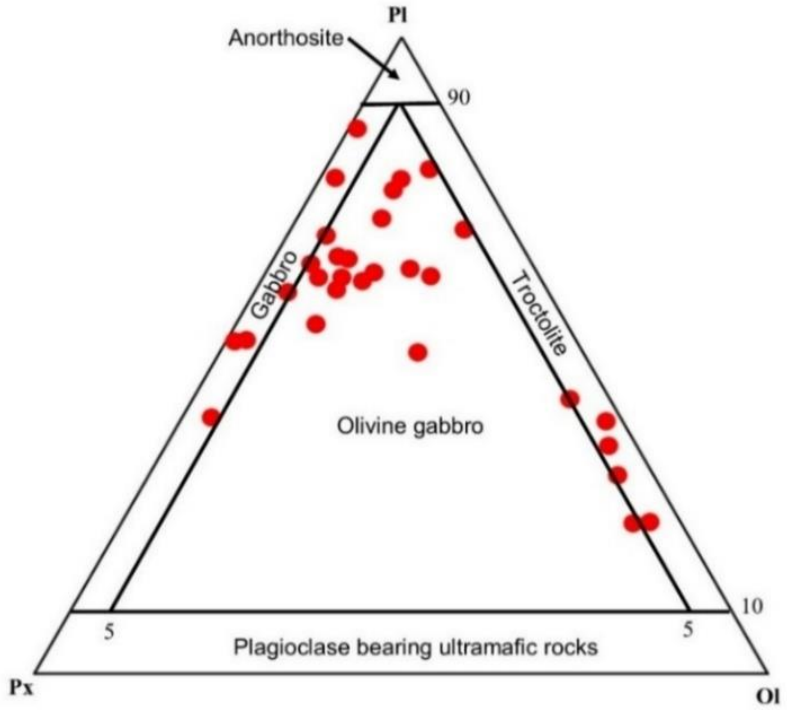

Fig.3. Classification of the studied mafic rocks of the Bulfat Complex according to (Streckeisen, 1974; Streckeisen, 1976)

Table 1. Modal mineral composition of the studied mafic rocks of the Bulfat Complex

Rock name	Sample	Primary Minerals				Amph	Opaque Minerals	Secondary Minerals (Ser, Srp, Chl)	Other	Total
		Pl	Cpx	Opx	Ol					
Olivine Gabbro	K1	73	6		13	2	5	1		100
Troctolite	K2	26	4		53		5	12		100
Troctolite	K3	28	3		47		6	11	5	100
Olivine gabbro	K4	56	14	1	17	4	7	1		100
Olivine gabbro	K5	55	13		20	5	4	3		100
Troctolite	K6	17	3		51		7	18	4	100
Troctolite	K7	24	3	1	53	5	7	5	2	100
Olivine gabbro	K8	65	6		22		7	0		100
Olivine Gabbro	K9	45	19	1	24	5	3	2	1	100
Olivine gabbro	K10	55	25	1	10	5	2	2		100
Gabbro	K11	44	39		2		3	4	8	100
Gabbro	K12	41	34	1	2		4	13	5	100
Olivine gabbro	K13	68	16		11		5	0		100
Olivine gabbro	K14	60	21		14		5	0		100
Olivine gabbro	K15	58	22		9	2	7	2		100
Olivine gabbro	K16	70	12		10	3	5	0		100
Gabbro	K17	40	55		4		1	0		100
Olivine gabbro	K18	50	31		10		7	2		100
Olivine gabbro	K19	58	25		10		6	1		100
Olivine gabbro	K20	70	10		10		5	3	2	100
Troctolite	K21	35	3		51		8	3		100
Olivine gabbro	K22	58	23		13		3	0	3	100
Gabbro	K23	54	32		4	5	4	1		100
Troctolite	K24	35	3		38	3	5	11	5	100
Gabbro	K25	78	12		1		3	1	5	100
Gabbro	K26	74	19		2		1	0	4	100
Olivine gabbro	K27	64	24		5	5	1	0	1	100
Olivine gabbro	K28	61	24		8	5	1	0	1	100
Olivine gabbro	K29	60	28		5	5	1	0	1	100
Olivine gabbro	K30	58	28		7	5	1	0	1	100

Pl: Plagioclase, Cpx: Clinopyroxene, Opx: Orthopyroxene, Ol: Olivine, Amph: Amphibole, Ser: Sericite, Srp: Serpentine, Ch: Chlorite.

4.1.2. Gabbro

The studied gabbro varies from dark to light grey, consists of plagioclase (40-78%) and clinopyroxene (12-55%) as essential minerals, along with minor olivine (1-4%), orthopyroxene (0-1%), and opaque minerals (1-4%) (Fig. 4E). Grain sizes are usually medium to coarse grained, rarely fine grain size observed (<1 mm) classified as dolerite and a very coarse (> 2.5 cm) classified as gabbroic pegmatite (Buday and Jassim, 1987; Al-Hamed et al., 2019).

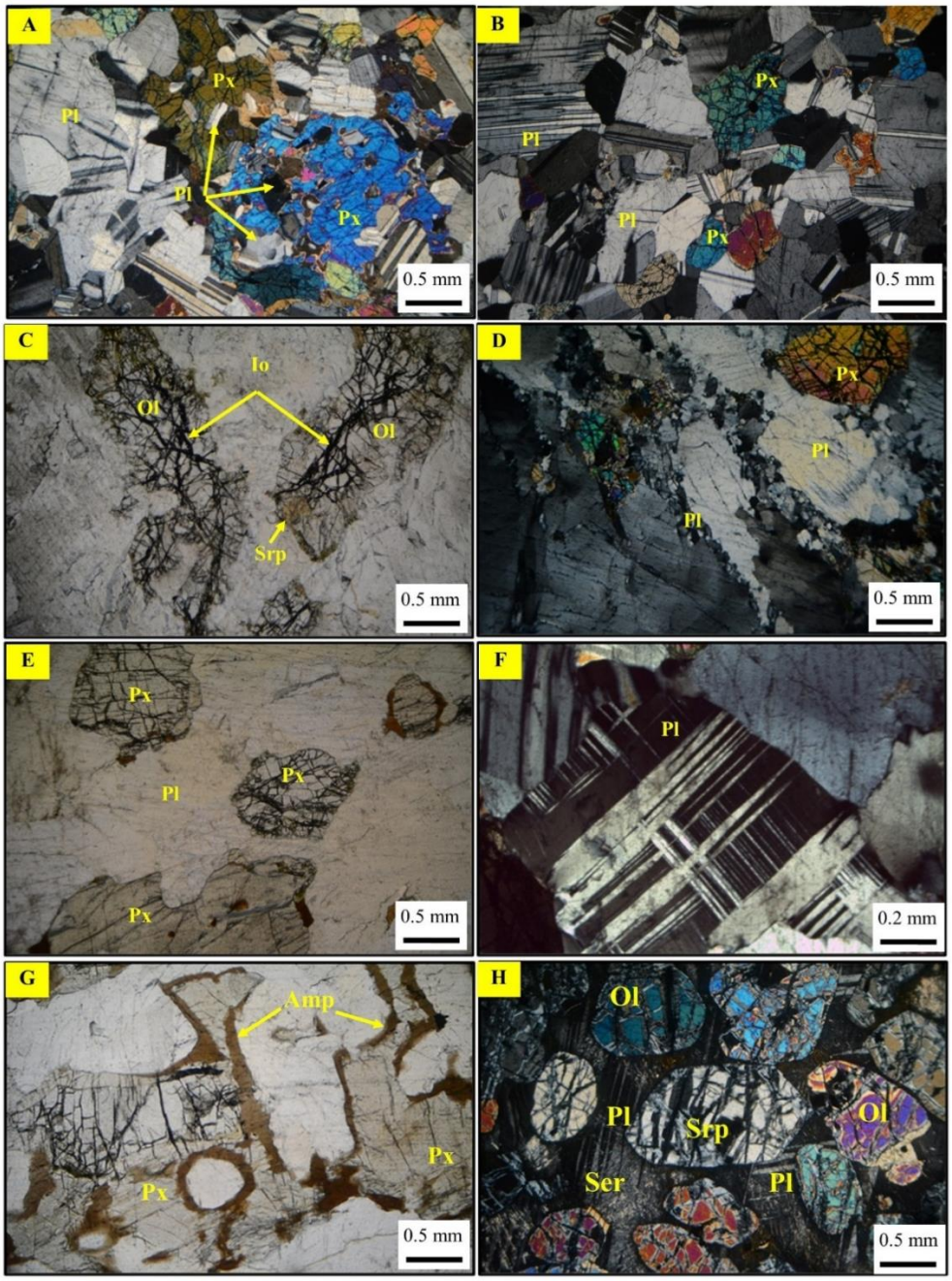

Fig.4. Photomicrographs of thin sections of the studied mafic rocks of the Bulfat Complex: A) Olivine gabbro rock showing poikilitic texture (XPL and 4X), sample (K8); B) Ophitic texture (XPL and 4X), sample (K13); C) Olivine grains with black iron oxides (Io) inside the cracks and has alteration at the grain margin (PPL and 4X), sample (K10); D) Porphyroclastic texture (XPL and 4X), sample (K11); E) Gabbro rock sample with interstitial pyroxene grains between plagioclase (PPL and 4X), sample (K26); F) Chessboard twinning (XPL and 10X), sample (K12); G) Corona texture in gabbro (PPL and 4X), sample (K23), and H) Troctolite rock (XPL and 4X), sample (K7)

Plagioclase (0.5-6 mm) is subhedral to anhedral, displaying polysynthetic and chessboard twinning (Fig. 4F), with deformation features like bent or fractured twins, rarely altered to sericite. Plagioclase has an extinction angle of 30°. Clinopyroxene (0.5-3 mm) is mostly subhedral to anhedral in shape and appears as elongated to short prisms. Olivine (0.5-2 mm) occurs interstitially among plagioclase and clinopyroxene grains with irregular fractures, rarely altered to serpentine. Among the accessory minerals

observed in the studied gabbro are amphibole, pyrrhotite, and chalcopyrite. Additionally, secondary chlorite is also noted in a few samples.

The rock exhibits hypidiomorphic granular, poikilitic, ophitic to subophitic, corona textures (Fig. 4G) and porphyroclastic textures.

4.1.3. Troctolite

This rock consists mainly of olivine (38-53%) and plagioclase (17-35%), with minor clinopyroxene (3-4%), orthopyroxene (0-1%), amphibole (0-5%), and opaque minerals (5-8%). It is medium grain size (0.5-5 mm) (Fig. 4H).

Olivine (0.5-2 mm) is an anhedral mineral that forms the majority of rock samples and has fractures filled with serpentine and Fe-oxides. Olivine contains inclusions of spinel and sulphide minerals (pyrrhotite and pentlandite) (Fig. 5B). Olivine displays a decumulate texture indicative of its early crystallization from magma; it shows serpentinization (Fig. 4H). Plagioclase (1-4 mm) occurs as subhedral to anhedral laths with polysynthetic twinning, shows intercumulate texture, and has extinction angles between 40° and 45°, which in some samples show complete sericitization (Fig. 4H). Pyroxene is present in small quantities, primarily as clinopyroxene, with occasional occurrences of orthopyroxene, and appears as subhedral to anhedral grains (1-5 mm). Some grains alter to amphibole (Fig. 4G). Clinopyroxene contains exsolution lamellae of amphibole and Cr-rich spinel. Opaque minerals often surround olivine cracks. Accessory minerals include Cr-rich spinel, which appears as green anhedral grains under plane polarized light (PPL), and apatite is observed in some samples.The troctolite rock type exhibits hypidiomorphic granular, ophitic, exsolution, and mesh textures.

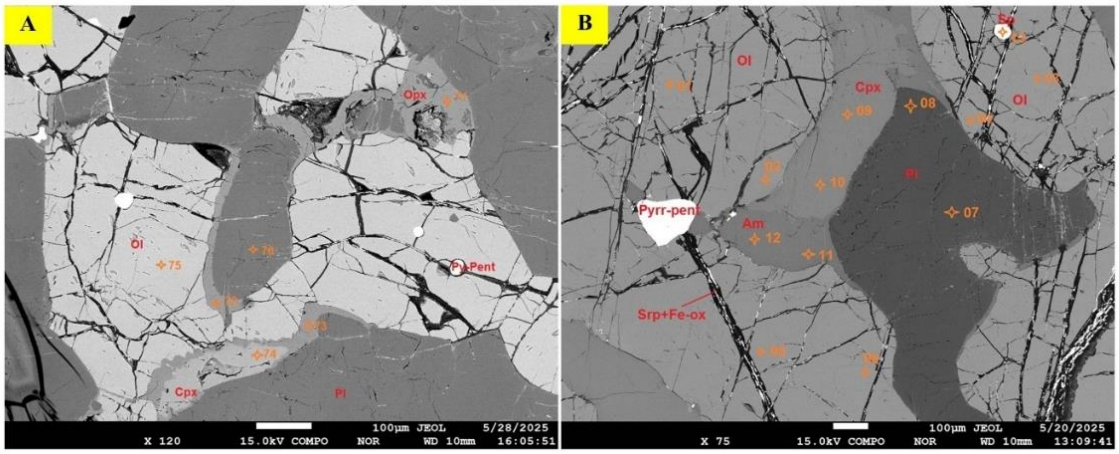

Fig. 5. Backscatter images (BSE) of: A) Sulphide (pyrrhotite-pentlandite) inclusions in olivine. Orthopyroxene surrounding olivine, sample (K4); and B) Plagioclase, clinopyroxene, and amphibole between olivine crystals. Inclusions of sulphides (pentlandite, pyrrhotite) and spinel in olivine. Olivine fractures filled with serpentine and Fe-oxides, sample (K7)

4.2. Mineral Chemistry

The chemical compositions of minerals were analyzed in three representative samples from gabbro, olivine gabbro, and troctolite rock types. Mineral chemistry was determined using Electron Probe Micro Analysis (EPMA).

The mineral chemistry of plagioclase in the studied mafic rocks shows compositional variation (Table 2, Fig. 6A). Plagioclase in the troctolite sample is more calcic and bytownite in composition (An75-An62), while plagioclase in the olivine gabbro and gabbro samples falls within the labradorite field (An56-An61) and (An55-57), respectively.

Table 2. Average composition of plagioclase in mafic rocks from the Bulfat Complex, northeast of Iraq. The formula is calculated based on 32 oxygen atoms

Rock type	**Olivine gabbro (K4)**							**Gabbro (K11)**						**Troctolite (K7)**								
Analysis spot	7	8	20	29	30	31	32	72	73	74	85	86	93	37	40	53	54	56	57	58	59	70
SiO_2	54.0	52.4	54.2	53.5	53.1	53.8	52.6	54.6	54.6	54.6	54.5	54.5	54.1	49.5	49.2	49.2	48.4	48.3	49.7	50.7	46.9	48.6
TiO_2	0.0	0.0	0.0	0.0	0.0	0.0	0.0	0.0	0.0	0.0	0.0	0.0	0.0	0.0	0.0	0.1	0.0	0.0	0.1	0.0	0.0	0.0
Al_2O_3	29.9	29.5	29.7	30.0	30.0	29.9	30.3	30.3	30.3	30.2	30.2	30.2	30.3	32.4	32.7	32.4	33.0	33.1	31.9	31.7	33.5	32.6
FeO	0.0	0.4	0.1	0.1	0.1	0.1	0.1	0.1	0.1	0.1	0.1	0.1	0.1	0.1	0.1	0.1	0.1	0.0	0.1	0.1	0.1	0.2
MnO	0.0	0.1	0.0	0.0	0.0	0.0	0.0	0.0	0.0	0.0	0.0	0.0	0.0	0.0	0.0	0.0	0.0	0.0	0.0	0.0	0.0	0.0
MgO	0.0	0.1	0.0	0.0	0.0	0.0	0.0	0.1	0.1	0.1	0.1	0.1	0.1	0.0	0.0	0.0	0.0	0.0	0.0	0.0	0.0	0.0
CaO	11.6	12.4	11.3	11.8	12.4	11.9	12.7	10.2	10.4	10.5	10.6	10.7	10.4	14.8	15.1	15.0	15.2	15.8	14.2	13.9	16.4	15.1
Na_2O	4.6	4.2	4.7	4.2	4.6	4.4	4.3	4.7	4.5	4.6	4.4	4.2	4.5	2.7	2.6	2.6	2.4	2.1	2.9	3.2	1.7	2.6
K_2O	0.1	0.0	0.0	0.0	0.0	0.0	0.0	0.0	0.0	0.0	0.0	0.0	0.0	0.0	0.0	0.0	0.0	0.0	0.0	0.1	0.0	0.0
Sum	100.2	99.2	100.0	99.7	100.1	100.1	100.1	100.1	100.0	100.1	100.0	99.9	99.5	99.5	99.8	99.4	99.1	99.4	98.9	99.7	98.7	99.1
Si	9.8	9.6	9.8	9.7	9.6	9.7	9.5	9.9	9.9	9.9	9.9	9.9	9.9	9.1	9.0	9.0	8.9	8.9	9.2	9.3	8.7	9.0
Ti	0.0	0.0	0.0	0.0	0.0	0.0	0.0	0.0	0.0	0.0	0.0	0.0	0.0	0.0	0.0	0.0	0.0	0.0	0.0	0.0	0.0	0.0
Al	4.8	4.8	4.7	4.8	4.8	4.8	4.9	4.8	4.8	4.8	4.8	4.8	4.8	5.3	5.3	5.3	5.4	5.4	5.2	5.1	5.5	5.3
Fe(ii)	0.0	0.0	0.0	0.0	0.0	0.0	0.0	0.0	0.0	0.0	0.0	0.0	0.0	0.0	0.0	0.0	0.0	0.0	0.0	0.0	0.0	0.0
Mn	0.0	0.0	0.0	0.0	0.0	0.0	0.0	0.0	0.0	0.0	0.0	0.0	0.0	0.0	0.0	0.0	0.0	0.0	0.0	0.0	0.0	0.0
Mg	0.0	0.0	0.0	0.0	0.0	0.0	0.0	0.0	0.0	0.0	0.0	0.0	0.0	0.0	0.0	0.0	0.0	0.0	0.0	0.0	0.0	0.0
Ca	1.1	1.2	1.1	1.1	1.2	1.2	1.2	1.0	1.0	1.0	1.0	1.0	1.0	1.5	1.5	1.5	1.5	1.6	1.4	1.4	1.6	1.5
Na	0.4	0.4	0.4	0.4	0.4	0.4	0.4	0.4	0.4	0.4	0.4	0.4	0.4	0.2	0.2	0.2	0.2	0.2	0.3	0.3	0.2	0.2
K	0.0	0.0	0.0	0.0	0.0	0.0	0.0	0.0	0.0	0.0	0.0	0.0	0.0	0.0	0.0	0.0	0.0	0.0	0.0	0.0	0.0	0.0
Sum	16.1	16.0	16.1	16.1	16.0	16.1	16.0	16.2	16.2	16.2	16.2	16.2	16.2	16.1	16.1	16.1	16.1	16.1	16.1	16.1	16.0	16.0
An	57.7	60.9	56.7	59.7	60.2	58.9	61.9	55.9	56.4	56.8	57.2	57.5	56.5	74.6	76.1	75.6	77.5	80.2	72.4	70.0	83.4	76.3
Ab	41.9	38.9	43.2	40.1	39.7	41.1	38.0	44.0	43.5	43.1	42.7	42.4	43.4	25.2	23.8	24.1	22.2	19.7	27.3	29.6	16.5	23.6
Or	0.4	0.2	0.1	0.2	0.1	0.0	0.1	0.1	0.1	0.1	0.1	0.1	0.1	0.2	0.2	0.3	0.2	0.1	0.3	0.4	0.1	0.1
Sum	100.0	100.0	100.0	100.0	100.0	100.0	100.0	100.0	100.0	100.0	100.0	100.0	100.0	100.0	100.0	100.0	100.0	100.0	100.0	100.0	100.0	100.0

The mineral chemistry of pyroxene in the studied mafic rocks reveals two main types: clinopyroxene and orthopyroxene. Clinopyroxene is classified as diopside with average compositions of $Wo_{46}En_{46}Fs_8$. Orthopyroxene is classified as enstatite (Table 3, Fig. 6B).

The mineral chemistry of olivine has average forsterite (Fo) contents of Fo 77 in troctolite, Fo 76 in olivine gabbro, and Fo 75 in gabbro, placing them within the chrysolite range (Table 4, Fig. 6C).

Amphibole in the studied mafic rocks occurs mainly as secondary calcic amphibole, with compositions dominated by pargasite (Table 5, Fig. 6D). Moreover, opaque minerals in the studied mafic rocks include Cr-rich spinel/chromite and Fe-oxides as well as an assemblage of sulphides (pyrrhotite, pentlandite, chalcopyrite, and rare sphalerite). Alteration products such as serpentine, chlorite, and sericite were also observed.

Table 3. Average composition of pyroxene in mafic rocks from the Bulfat Complex, northeast of Iraq. The formula is calculated based on 6 oxygen atoms

Rock type	**Olivine gabbro (K4)**								**Gabbro (K11)**							**Troctolite (K7)**									
Analysis spot	47	48	51	52	71	72	73	74	88	89	90	98	99	105	106	9	10	14	16	18	21	22	23	26	38
SiO_2	52.9	53.1	53.2	54.2	55.4	56.0	55.7	53.3	52.1	52.5	52.3	53.1	52.5	54.20	53.70	52.4	52.6	52.1	52.0	55.8	56.2	55.1	56.0	54.4	52.4
TiO_2	0.6	0.5	0.4	0.1	0.0	0.0	0.0	0.3	0.8	0.8	0.9	0.7	0.8	0.12	0.15	1.0	0.6	0.9	1.1	0.2	0.1	0.0	0.1	0.4	1.0
Al_2O_3	2.9	2.9	2.6	1.5	1.1	1.0	1.0	1.9	3.6	3.5	3.7	2.5	2.5	1.45	1.60	3.1	2.4	3.9	4.0	1.0	0.9	0.1	0.9	1.5	2.7
Cr_2O_3	0.7	0.8	0.5	0.0	0.0	0.0	0.0	0.1	0.1	0.1	0.1	0.3	0.2	0.25	0.20	0.6	0.4	0.8	0.5	0.1	0.0	0.0	0.0	0.2	0.5
FeO	4.7	4.5	4.3	4.4	4.7	4.5	4.3	4.3	4.3	6.2	5.8	6.1	6.2	12.10	11.80	4.9	5.1	4.4	4.8	13.3	13.5	18.7	13.5	4.7	4.9
MnO	0.1	0.2	0.2	0.2	0.4	0.4	0.4	0.2	0.2	0.2	0.2	0.2	0.2	0.30	0.28	0.2	0.2	0.1	0.1	0.4	0.4	0.3	0.4	0.2	0.2
MgO	15.5	15.5	15.8	16.6	29.6	29.5	29.6	16.0	14.7	14.8	14.7	15.0	15.0	31.20	31.80	15.3	15.4	14.8	15.4	29.0	29.0	26.3	29.2	16.4	15.4
CaO	21.8	22.2	22.0	22.3	0.3	0.4	0.5	22.3	21.8	21.6	21.7	21.6	21.4	0.95	0.85	21.6	21.4	22.1	21.4	0.6	0.6	0.1	0.6	22.0	21.8
Na_2O	0.4	0.4	0.4	0.3	0.0	0.0	0.0	0.3	0.5	0.5	0.5	0.6	0.6	0.05	0.07	0.6	0.4	0.5	0.7	0.0	0.0	0.0	0.0	0.3	0.5
K_2O	0.0	0.0	0.0	0.0	0.0	0.0	0.0	0.0	0.0	0.0	0.0	0.0	0.0	0.02	0.01	0.0	0.0	0.0	0.0	0.0	0.0	0.0	0.0	0.0	0.0
Sum	99.6	100.0	99.3	99.5	91.4	91.9	91.5	98.8	98.2	100.2	99.9	100.2	99.3	100.64	100.46	99.6	98.4	99.7	99.9	100.5	100.7	100.5	100.8	100.1	99.5
Si	1.9	1.9	2.0	2.0	2.0	2.0	2.0	2.0	1.9	1.9	1.9	1.9	1.9	1.92	1.90	1.9	2.0	1.9	1.9	2.0	2.0	2.0	2.0	2.0	1.9
Al	0.1	0.1	0.0	0.0	0.0	0.0	0.0	0.0	0.1	0.1	0.1	0.1	0.1	0.06	0.07	0.1	0.0	0.1	0.1	0.0	0.0	0.0	0.0	0.0	0.1
Al	0.1	0.1	0.1	0.0	0.0	0.0	0.0	0.0	0.1	0.1	0.1	0.1	0.1	0.00	0.00	0.1	0.1	0.1	0.1	0.0	0.0	0.0	0.0	0.0	0.0
Fe(iii)	0.0	0.0	0.0	0.0	0.0	0.0	0.0	0.0	0.0	0.0	0.0	0.0	0.0	0.14	0.17	0.0	0.0	0.0	0.0	0.0	0.0	0.0	0.0	0.0	0.0
Cr	0.0	0.0	0.0	0.0	0.0	0.0	0.0	0.0	0.0	0.0	0.0	0.0	0.0	0.01	0.01	0.0	0.0	0.0	0.0	0.0	0.0	0.0	0.0	0.0	0.0
Ti	0.0	0.0	0.0	0.0	0.0	0.0	0.0	0.0	0.0	0.0	0.0	0.0	0.0	0.00	0.00	0.0	0.0	0.0	0.0	0.0	0.0	0.0	0.0	0.0	0.0
Fe(ii)	0.1	0.1	0.1	0.1	0.4	0.4	0.4	0.1	0.2	0.2	0.2	0.2	0.2	0.22	0.17	0.2	0.2	0.1	0.1	0.4	0.4	0.6	0.4	0.1	0.2
Mn	0.0	0.0	0.0	0.0	0.0	0.0	0.0	0.0	0.0	0.0	0.0	0.0	0.0	0.01	0.01	0.0	0.0	0.0	0.0	0.0	0.0	0.0	0.0	0.0	0.0
Mg	0.8	0.8	0.9	0.9	1.6	1.6	1.6	0.9	0.8	0.8	0.8	0.8	0.8	1.65	1.68	0.8	0.9	0.8	0.8	1.5	1.5	1.4	1.5	0.9	0.8
Ca	0.9	0.9	0.9	0.9	0.0	0.0	0.0	0.9	0.9	0.8	0.9	0.8	0.8	0.04	0.03	0.9	0.9	0.9	0.8	0.0	0.0	0.0	0.0	0.9	0.9
Na	0.0	0.0	0.0	0.0	0.0	0.0	0.0	0.0	0.0	0.0	0.0	0.0	0.0	0.00	0.00	0.0	0.0	0.0	0.0	0.0	0.0	0.0	0.0	0.0	0.0
K	0.0	0.0	0.0	0.0	0.0	0.0	0.0	0.0	0.0	0.0	0.0	0.0	0.0	0.00	0.00	0.0	0.0	0.0	0.0	0.0	0.0	0.0	0.0	0.0	0.0
Sum	4.0	4.0	4.0	4.0	4.0	4.0	4.0	4.0	4.0	4.0	4.0	4.0	4.0	4.04	4.05	4.0	4.0	4.0	4.0	4.0	4.0	4.0	4.0	4.0	4.0
Wo	46.3	46.8	46.3	45.6	0.6	0.9	0.9	46.2	46.3	45.7	46.2	45.5	45.3	1.76	1.56	46.2	45.5	47.8	45.8	1.1	1.2	0.1	1.2	45.2	46.2
En	45.7	45.5	46.2	47.1	79.2	79.0	79.7	46.3	43.4	43.6	43.6	44.1	44.2	80.49	81.34	45.4	45.5	44.5	45.9	78.1	77.8	71.0	78.0	47.0	45.3
Fs	8.0	7.7	7.5	7.3	20.2	20.2	19.4	7.5	10.3	10.6	10.2	10.4	10.5	17.75	17.09	8.5	8.9	7.7	8.3	20.8	20.9	28.8	20.8	7.8	8.5
Sum	100	100	100	100	100	100	100	100	100	100	100	100	100	100	100	100	100	100	100	100	100	100	100	100	100

Table 4. Average composition of olivine in mafic rocks from the Bulfat Complex, northeast of Iraq. The formula is calculated based on 4 oxygen atoms

Rock type	**Troctolite (K7)**							**Gabbro (K11)**						**Olivine gabbro (K4)**									
Analysis spot	41	42	43	44	45	66	67	84	85	86	87	101	102	1	2	3	4	5	19	25	27	28	43
SiO_2	38.9	38.4	38.8	39.3	38.8	39.0	39.0	40.2	38.1	38.9	39.5	38.1	38.3	38.6	38.7	38.9	38.7	38.8	38.6	38.9	39.1	55.5	38.7
TiO_2	0.0	0.0	0.0	0.0	0.0	0.0	0.0	0.0	0.0	0.0	0.0	0.0	0.0	0.0	0.0	0.1	0.0	0.0	0.0	0.0	0.0	0.2	0.0
Al_2O_3	0.0	0.0	0.0	0.0	0.0	0.0	0.0	0.0	0.0	0.0	0.0	0.0	0.0	0.0	0.0	0.0	0.0	0.0	0.0	0.0	0.0	1.2	0.0
Cr_2O_3	0.0	0.0	0.0	0.0	0.0	0.0	0.0	0.0	0.0	0.0	0.0	0.0	0.0	0.0	0.0	0.0	0.0	0.0	0.0	0.0	0.0	0.1	0.0
FeO	20.9	20.5	21.0	20.3	20.7	21.0	21.2	22.0	23.2	22.2	22.6	22.1	22.6	21.5	21.6	21.8	22.0	21.5	21.8	21.8	22.1	13.5	22.2
MnO	0.3	0.3	0.4	0.4	0.4	0.3	0.3	0.4	0.4	0.4	0.4	0.4	0.4	0.4	0.4	0.4	0.3	0.4	0.4	0.4	0.4	0.4	0.4
MgO	40.4	39.8	39.4	39.8	40.2	39.8	40.0	37.0	38.1	39.2	38.1	39.5	39.1	38.8	39.4	39.3	38.8	39.1	39.0	39.2	38.9	28.8	38.9
NiO	0.1	0.2	0.1	0.1	0.1	0.1	0.1	0.1	0.1	0.1	0.1	0.2	0.2	0.1	0.2	0.1	0.1	0.2	0.1	0.2	0.1	0.0	0.1
CaO	0.0	0.0	0.0	0.0	0.0	0.0	0.0	0.0	0.0	0.0	0.0	0.0	0.0	0.0	0.0	0.0	0.0	0.0	0.0	0.0	0.0	0.7	0.0
Sum	100.7	99.3	99.8	100.0	100.2	100.3	100.7	99.7	99.9	100.8	100.7	100.3	100.6	99.5	100.3	100.6	100.1	99.9	100.0	100.4	100.6	100.4	100.4
Si	1.0	1.0	1.0	1.0	1.0	1.0	1.0	1.0	1.0	1.0	1.0	1.0	1.0	1.0	1.0	1.0	1.0	1.0	1.0	1.0	1.0	1.3	1.0
Ti	0.0	0.0	0.0	0.0	0.0	0.0	0.0	0.0	0.0	0.0	0.0	0.0	0.0	0.0	0.0	0.0	0.0	0.0	0.0	0.0	0.0	0.0	0.0
Al	0.0	0.0	0.0	0.0	0.0	0.0	0.0	0.0	0.0	0.0	0.0	0.0	0.0	0.0	0.0	0.0	0.0	0.0	0.0	0.0	0.0	0.0	0.0
Cr	0.0	0.0	0.0	0.0	0.0	0.0	0.0	0.0	0.0	0.0	0.0	0.0	0.0	0.0	0.0	0.0	0.0	0.0	0.0	0.0	0.0	0.0	0.0
Fe(ii)	0.4	0.4	0.5	0.4	0.4	0.5	0.5	0.5	0.5	0.5	0.5	0.5	0.5	0.5	0.5	0.5	0.5	0.5	0.5	0.5	0.5	0.3	0.5
Mn	0.0	0.0	0.0	0.0	0.0	0.0	0.0	0.0	0.0	0.0	0.0	0.0	0.0	0.0	0.0	0.0	0.0	0.0	0.0	0.0	0.0	0.0	0.0
Mg	1.5	1.5	1.5	1.5	1.5	1.5	1.5	1.4	1.5	1.5	1.5	1.5	1.5	1.5	1.5	1.5	1.5	1.5	1.5	1.5	1.5	1.0	1.5
Ni	0.0	0.0	0.0	0.0	0.0	0.0	0.0	0.0	0.0	0.0	0.0	0.0	0.0	0.0	0.0	0.0	0.0	0.0	0.0	0.0	0.0	0.0	0.0
Ca	0.0	0.0	0.0	0.0	0.0	0.0	0.0	0.0	0.0	0.0	0.0	0.0	0.0	0.0	0.0	0.0	0.0	0.0	0.0	0.0	0.0	0.0	0.0
Sum	3.0	3.0	3.0	3.0	3.0	3.0	3.0	3.0	3.0	3.0	3.0	3.0	3.0	3.0	3.0	3.0	3.0	3.0	3.0	3.0	3.0	2.7	3.0
Fo	77.2	77.3	76.7	77.4	77.3	76.9	76.8	74.7	74.3	75.6	74.7	75.8	75.2	75.9	76.2	75.9	75.6	76.2	75.8	75.9	75.5	78.7	75.4
Fa	22.5	22.3	22.9	22.2	22.3	22.8	22.8	24.9	25.4	24.0	24.9	23.8	24.4	23.6	23.5	23.6	24.0	23.4	23.8	23.7	24.0	20.7	24.2
Tp	0.3	0.4	0.4	0.4	0.4	0.4	0.4	0.4	0.4	0.4	0.4	0.4	0.4	0.5	0.4	0.4	0.4	0.4	0.4	0.4	0.4	0.6	0.5
Sum	100.0	100.0	100.0	100.0	100.0	100.0	100.0	100.0	100.0	100.0	100.0	100.0	100.0	100.0	100.0	100.0	100.0	100.0	100.0	100.0	100.0	100.0	100.0

Table 5. Average composition of amphibole in mafic rocks from the Bulfat Complex, northeast of Iraq. The formula is calculated based on 23 oxygen atoms

Rock type	**Olivine gabbro (K4)**					**Troctolite (K7)**					**Gabbro (K11)**			
Analysis spot	60	61	62	63	65	11	12	15	36	39	82	83	84	91
SiO_2	43.94	43.83	43.81	43.80	43.12	43.61	43.44	43.42	43.74	43.35	44.75	44.38	44.88	44.26
TiO_2	1.94	1.63	1.44	1.90	2.01	2.66	2.98	3.46	2.16	3.86	1.50	2.02	1.96	1.64
Al_2O_3	12.56	13.32	12.58	13.14	13.06	12.18	12.16	11.82	12.78	11.02	13.35	12.45	12.45	12.63
FeO	7.15	6.82	6.98	6.89	6.89	7.13	7.28	7.32	7.24	7.68	4.32	6.76	4.26	4.18
MnO	0.11	0.14	0.14	0.09	0.07	0.14	0.11	0.12	0.08	0.13	0.09	0.14	0.08	0.15
MgO	15.60	16.05	16.35	16.21	15.93	15.59	15.59	14.92	15.64	14.85	17.86	16.72	17.64	17.48
CaO	11.66	11.44	11.65	11.61	11.42	11.18	11.22	11.50	11.38	11.28	11.14	11.18	11.31	10.92
Na_2O	2.48	2.51	2.44	2.54	2.70	2.88	2.90	2.94	2.75	2.97	2.91	2.53	2.66	2.84
K_2O	0.66	0.67	0.65	0.61	0.63	0.33	0.33	0.22	0.27	0.19	0.36	0.59	0.38	0.34
Cr_2O_3	0.56	0.24	0.26	0.10	0.10	0.75	0.92	1.46	0.69	1.22	0.95	0.12	1.18	1.82
Total	96.67	96.65	96.30	96.88	95.94	96.45	96.92	97.18	96.72	96.55	97.22	96.88	96.80	96.25
T: Si	6.35	6.28	6.31	6.27	6.25	6.31	6.26	6.30	6.29	6.34	6.28	6.32	6.35	6.29
Al (iv)	1.65	1.72	1.69	1.73	1.75	1.69	1.74	1.70	1.71	1.66	1.72	1.68	1.65	1.71
Fe(iii)	0.00	0.00	0.00	0.00	0.00	0.00	0.00	0.00	0.00	0.00	0.00	0.00	0.00	0.00
Ti	0.00	0.00	0.00	0.00	0.00	0.00	0.00	0.00	0.00	0.00	0.00	0.00	0.00	0.00
C: Al (vi)	0.49	0.53	0.45	0.49	0.48	0.38	0.33	0.32	0.45	0.24	0.49	0.40	0.43	0.40
Ti	0.21	0.18	0.16	0.20	0.22	0.29	0.32	0.38	0.23	0.42	0.16	0.22	0.21	0.18
Fe(iii)	0.25	0.47	0.50	0.44	0.39	0.31	0.32	0.01	0.39	0.01	0.61	0.62	0.45	0.58
Mg	3.36	3.43	3.51	3.46	3.44	3.36	3.35	3.23	3.35	3.24	3.73	3.55	3.72	3.70
Fe(ii)	0.62	0.35	0.34	0.38	0.44	0.55	0.56	0.88	0.48	0.92	-0.10	0.18	0.06	-0.09
Ca	0.00	0.00	0.00	0.00	0.00	0.00	0.00	0.00	0.00	0.00	0.00	0.00	0.00	0.00
B: Ca	1.81	1.76	1.80	1.78	1.77	1.73	1.73	1.79	1.75	1.77	1.67	1.70	1.71	1.66
Na	0.19	0.24	0.20	0.22	0.23	0.27	0.27	0.21	0.25	0.23	0.33	0.30	0.29	0.34
A: Ca	0.00	0.00	0.00	0.00	0.00	0.00	0.00	0.00	0.00	0.00	0.00	0.00	0.00	0.00
Na	0.50	0.46	0.48	0.48	0.53	0.54	0.54	0.61	0.52	0.61	0.47	0.40	0.44	0.44
K	0.12	0.12	0.12	0.11	0.12	0.06	0.06	0.04	0.05	0.04	0.06	0.11	0.07	0.06
(Na+K)A	0.62	0.58	0.60	0.60	0.65	0.60	0.60	0.65	0.57	0.65	0.53	0.51	0.51	0.51
$Mg/(Mg+Fe^{2+})$	0.85	0.91	0.91	0.90	0.89	0.86	0.86	0.79	0.87	0.78	1.03	0.95	0.98	1.02

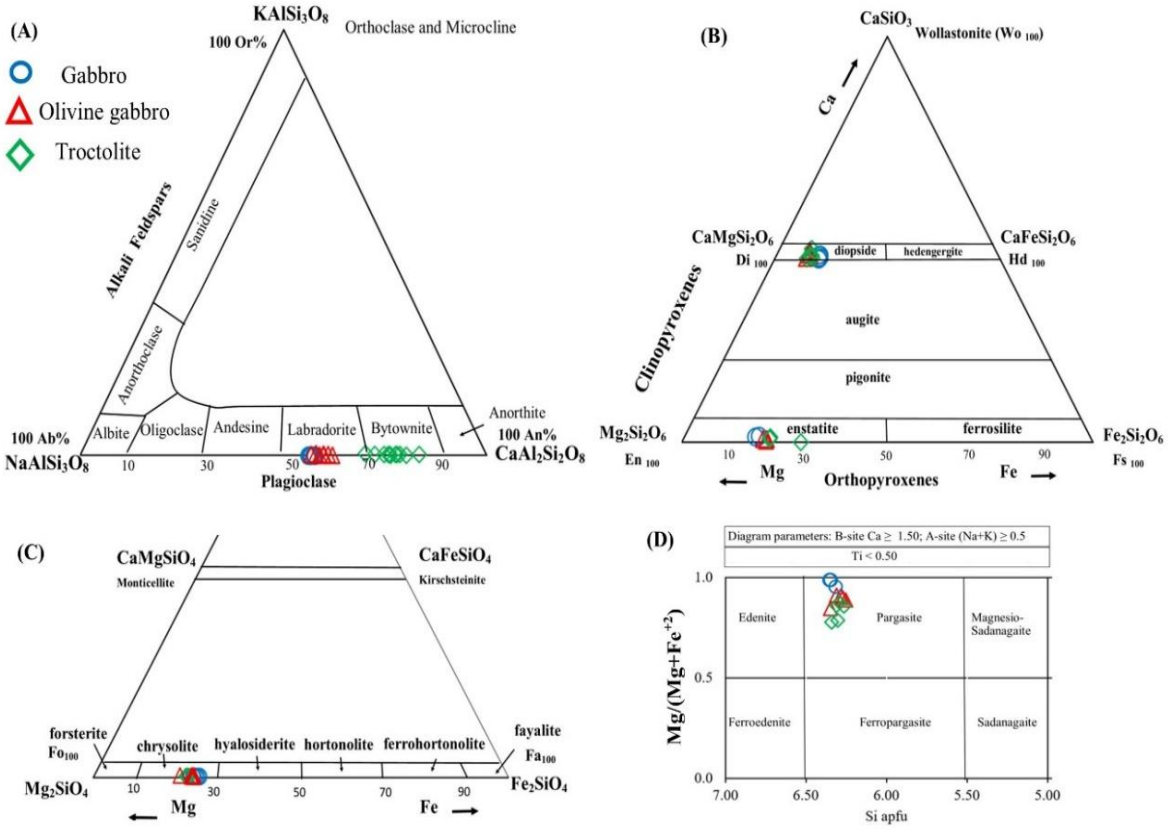

Fig. 6. Mineral chemistry classification diagram for the studied mafic rocks of the Bulfat Complex: A) Plagioclase classification plotted on the (Ab-An-Or) diagram (after Deer et al., 1992); B) Pyroxene classification plotted on (En-Wo-Fs) diagram (after Morimoto, 1988); C) Olivine classification plotted on (Fo forsterite Mg_2SiO_4, Tp tephroite Mn_2SiO_4, Fa fayalite Fe_2SiO_4) (after Poldervaart, 1950, and Winchell, 1951); and D) Calcic amphiboles classification (after Leake et al., 1997)

4.3. Bulk Chemical Analysis

The studied mafic rocks of the Bulfat Complex exhibit a wide range of compositional variations. The results show high SiO_2 (38.7 to 46.5 wt.%), MgO (8.4 to 29.6 wt.%), Al_2O_3 (4.2 to 22.6 wt.%), Fe2O3 (4.36-16.1 wt.%), and CaO (4.01-14.85 wt.%) and low contents of alkali elements (average Na_2O+K_2O=0.97 wt.%), and TiO_2=0.19 wt.% (Table 6). Their Mg# (100 Mg/[Mg + Fe^{2+}]) range from 69 to 75, indicating derivation from a relatively primitive mantle-related magma (Philpotts and Ague, 2009; Winter, 2014) (Table 6). Transition trace elements like Ni (201-998 ppm) and Co (33-111 ppm) are enriched in the studied mafic rocks and show strong correlations with MgO, with r=0.99 for both. Large ion lithophile elements (LILE), particularly Sr (76-426 ppm) and Ba (4.1-23.1 ppm), are enriched in the studied mafic rocks (Table 6) due to their mobility and ease of dissolution and transport from subducted crystal materials into the source rocks (Pearce, 1983; Zrary et al., 2022). The notable Sr enrichment may also reflect its substitution with Ca in calcic plagioclase (Mason and Moore, 1982). High field strength elements (HFSE) such as Zr (4-16 ppm), Hf (0.09-0.47 ppm), and Nb (0.06-0.28 ppm) are low in the studied mafic rocks (Table 6), due to their high incompatibility during the magmatic process. In the Middlemost (1994) diagram (SiO_2 vs. $Na_2O + K_2O$), the majority of samples were plotted in the gabbro field, with a few samples falling within peridot gabbro due to their low silica content, as they are mineralogically rich in olivine (Fig. 7A)

The studied rocks exhibit a calc-alkaline affinity. This is supported by the SiO_2 vs. Zr/TiO_2 diagram (Winchester and Floyd, 1977) (Fig. 7B), where all samples were plotted within sub-alkali basalt (Sub-

AB) and alkali basalt (AB). On the AFM diagram (Irvine and Baragar, 1971) (Fig. 7C), most samples were plotted within the calc-alkaline field with shifting toward the FeO and MgO fields due to their enrichment in Mg and Fe content. In the Al_2O_3-(FeO^t + TiO_2)-MgO diagram (Jensen, 1976) (Fig. 7D), the samples of gabbro and olivine gabbro were plotted within the calc-alkaline field, while the troctolite samples were plotted in the basaltic komatite field. Furthermore, the Al_2O_3 vs. SiO_2 composition of clinopyroxenes (Le Bas, 1962) (Fig. 7E) supports the subalkaline character of the rocks based on mineral chemistry.

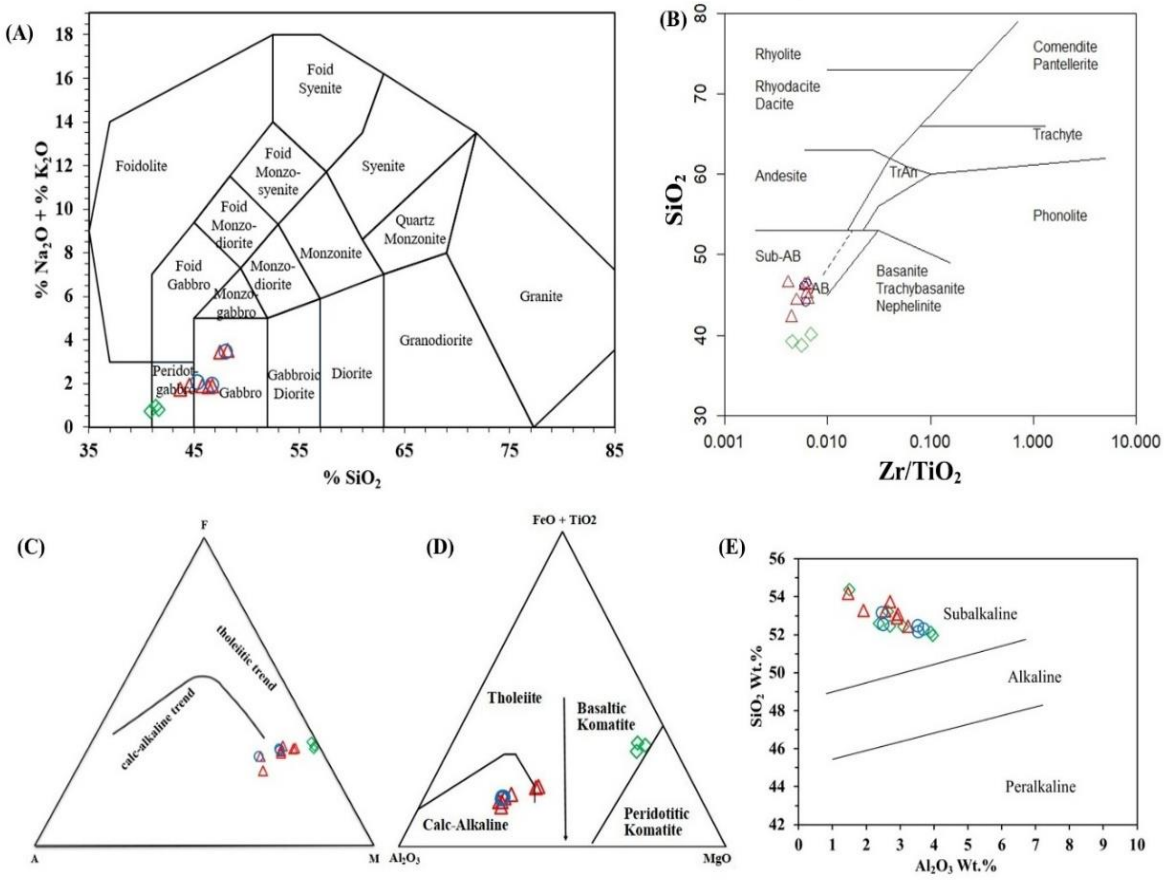

Fig.7. A) Total alkali-silica classification diagram (Middlemost, 1994); B) SiO_2 vs. Zr/TiO_2 diagram (Winchester and Floyd, 1977); C) AFM diagram (Irvine and Baragar, 1971); D) Al_2O_3- FeO^t + TiO_2-MgO diagram (Jensen, 1976); and E) SiO_2 (wt.%) vs. Al_2O_3 (wt.%) diagram for clinopyroxene crystal (Le Bas, 1962)

4.4. Rare Earth Elements (REE)

The total REE contents range from 7.63 to 12.57 ppm, with an average of 10.27 ppm. The chondrite REE patterns normalized to McDonough and Sun (1995) showed that the majority of the samples are enriched in LREE compared to HREE ((La/Sm)n=1.43), except troctolite samples exhibit LREE depletion relative to HREE with (La/Sm)n=0.60 (Fig. 8A), this suggests their early cumulate residues formed during fractional crystallization, as the accumulating solid phase (troctolite cumulate) slightly prefers HREEs over LREEs during crystallization (Rollinson, 1993). Additionally, the studied mafic rocks exhibit a positive Eu anomaly (Eu/Eu*=1.81-4.35); (Table 6 and Fig. 8), which suggests accumulation of Ca-rich plagioclase (Ottonello et al., 1984; Trubelja et al., 1995).

Table 6. Whole-rock geochemical analyses of the studied mafic rocks of the Bulfat Complex with major and minor oxides (wt.%), trace elements and REE (ppm)

Samples	K1	K4	K6	K7	K8	K9	K10	K11	K13	K14	K17	K19	K25
Rock type	Olivine gabbro	Olivine gabbro	Troctolite	Troctolite	Olivine gabbro	Troctolite	Olivine gabbro	Gabbro	Olivine gabbro	Olivine gabbro	Gabbro	Olivine gabbro	Gabbro
Major and minor oxides (wt%)													
SiO_2	46.3	44.3	38.7	39.2	42.2	40.1	44.5	46.5	46.5	46.2	46.1	45.1	44.2
TiO_2	0.25	0.08	0.25	0.29	0.09	0.19	0.14	0.24	0.17	0.25	0.17	0.16	0.18
Al_2O_3	22.6	20.4	4.2	5.2	20.4	6.2	21.5	22.1	22.2	22.5	22.3	22.5	21.9
Fe_2O_3	4.36	8.08	15.90	16.10	7.76	15.11	6.11	5.45	5.04	5.64	5.32	5.01	5.50
MnO	0.06	0.13	0.29	0.26	0.12	0.21	0.11	0.06	0.09	0.06	0.09	0.08	0.10
MgO	9.0	14.1	29.6	28.1	13.6	29.1	9.7	8.7	8.7	9.2	8.8	8.4	8.9
CaO	10.15	10.4	5.03	4.01	10.75	5.09	13.11	10.25	14.85	10.12	13.91	14.14	14.61
Na_2O	3.29	1.85	0.65	0.71	1.62	0.88	1.77	3.25	1.82	3.28	1.84	1.75	1.91
K_2O	0.08	0.06	0.03	0.04	0.07	0.03	0.06	0.07	0.06	0.08	0.06	0.05	0.06
P_2O_5	0.03	0.02	0.02	0.05	0.01	0.03	<0.01	0.03	<0.01	0.03	<0.01	<0.01	<0.01
Cr_2O_3	0.06	0.04	0.13	0.12	0.03	0.12	0.08	0.06	0.11	0.061	0.11	0.11	0.12
SrO	0.04	0.05	0.01	0.01	0.05	0.01	0.05	0.04	0.05	0.04	0.05	0.04	0.05
BaO	<0.01	<0.01	<0.01	<0.01	<0.01	<0.01	<0.01	<0.01	<0.01	<0.01	<0.01	<0.01	<0.01
LOI	1.94	0.99	1.22	1.45	2.14	1.34	1.51	1.93	1.11	1.95	1.12	1.08	1.14
Total	98.2	100.6	96.1	95.6	98.8	98.4	98.7	98.75	100.8	99.4	99.9	98.5	98.7
Mg#	75.71	71.48	71.71	70.45	71.27	72.60	69.55	70.65	71.44	71.11	70.42	70.74	69.95
Trace elements (ppm)													
Rb	1.1	0.9	0.4	0.3	1.1	0.6	0.6	1.0	0.2	1.0	0.2	0.4	0.2
Sr	365	377	76	85	395	77	410	360	426	368	420	405	410
Cs	0.08	0.08	0.03	0.01	0.11	0.02	0.06	0.07	0.02	0.08	0.02	0.019	0.021
Ba	13.8	23.1	4.1	5.2	20.1	6.4	20.2	13.5	20.8	14.5	20.6	19.2	21.9
Zr	16	4	14	13	4	13	9	15	7	15	10	10	11
Hf	0.4	0.09	0.47	0.45	0.15	0.39	0.2	0.39	0.26	0.42	0.26	0.25	0.27
Nb	0.28	<0.05	<0.05	<0.05	0.06	<0.05	<0.05	<0.05	<0.05	<0.05	<0.05	<0.05	<0.05
Ta	<0.1	<0.1	<0.1	<0.1	<0.1	<0.1	<0.1	<0.1	<0.1	<0.1	<0.1	<0.1	<0.1
Ti	1500	500	1500	1600	600	1300	800	1400	1100	1500	1100	1000	1200
W	<0.5	<0.5	<0.5	<0.5	<0.5	<0.5	<0.5	<0.5	<0.5	<0.5	<0.5	<0.5	<0.5
V	31	17	93	99	24	87	50	30	77	31	76	72	81
Cr	430	306	1050	950	259	970	500	420	804	435	795	770	820
Co	34	61	111	109	60	102	45.5	33	33	34	33	35	34
Ni	275	503	981	998	469	977	201	273	210	276	211	205	215
Zn	23	49	113	111	50	107	35	23	27	23	27	26	28
Th	<0.05	<0.05	<0.05	<0.05	0.05	<0.05	<0.05	<0.05	<0.05	<0.05	<0.05	<0.05	<0.05
U	<0.05	<0.05	<0.05	<0.05	<0.05	<0.05	<0.05	<0.05	<0.05	<0.05	<0.05	<0.05	<0.05
Ga	11.2	13.8	4.7	4.3	13.2	5.1	13.7	11	14.2	11.3	13.9	13.6	14.01
Y	3.4	1.6	4.5	4.8	4.9	4.3	5.5	4.8	1.6	3.9	4.3	4.5	4.6
Li	10	10	10	10	10	10	<10	10	<10	10	<10	<10	<10
REE (ppm)													
La	1.10	1.80	0.50	0.50	1.40	0.60	1.50	1.60	1.05	1.12	1.66	1.52	1.61
Ce	3.00	3.60	1.90	2.20	2.80	2.10	3.20	3.60	2.90	3.20	3.80	3.40	3.70
Pr	0.45	0.39	0.35	0.39	0.28	0.37	0.38	0.48	0.44	0.45	0.41	0.46	0.39
Nd	1.90	1.60	2.10	1.90	1.20	2.00	1.80	2.40	1.85	1.90	2.33	2.28	2.39
Sm	0.55	0.38	0.57	0.61	0.34	0.49	0.53	0.72	0.53	0.56	0.71	0.69	0.65
Eu	0.35	0.44	0.52	0.51	0.40	0.54	0.48	0.56	0.34	0.35	0.55	0.53	0.52
Gd	0.60	0.25	0.92	0.99	0.33	0.87	0.56	0.79	0.59	0.62	0.82	0.75	0.80
Tb	0.09	0.07	0.15	0.11	0.05	0.14	0.09	0.14	0.08	0.09	0.15	0.13	0.14
Dy	0.56	0.19	0.99	0.93	0.33	0.89	0.65	0.98	0.55	0.57	0.95	0.92	0.99
Ho	0.13	0.07	0.18	0.22	0.07	0.20	0.12	0.17	0.12	0.13	0.18	0.16	0.17
Er	0.35	0.19	0.57	0.61	0.23	0.59	0.32	0.41	0.34	0.35	0.43	0.39	0.42
Tm	0.07	0.03	0.09	0.07	0.04	0.08	0.05	0.07	0.06	0.07	0.08	0.06	0.07
Yb	0.35	0.18	0.58	0.58	0.14	0.51	0.28	0.42	0.34	0.35	0.44	0.40	0.42
Lu	0.05	0.02	0.09	0.11	0.02	0.07	0.04	0.06	0.05	0.05	0.06	0.05	0.06
∑REE	9.55	9.21	9.51	9.73	7.63	9.45	10.00	12.40	9.24	9.81	12.57	11.74	12.33
(Ce/Yb)n	2.25	5.25	0.86	1.00	5.25	1.08	3.00	2.25	2.24	2.40	2.27	2.23	2.31
(Gd/Yb)	1.16	0.94	1.08	1.16	1.60	1.16	1.36	1.28	1.18	1.20	1.27	1.27	1.29
(La/Sm)	1.25	2.96	0.55	0.51	2.57	0.76	1.77	1.39	1.24	1.25	1.46	1.38	1.55
(La/Yb)n	2.14	6.79	0.59	0.59	6.79	0.80	3.64	2.59	2.10	2.17	2.56	2.58	2.60
Eu/Eu*	1.86	4.35	2.19	2.00	3.64	2.52	2.69	2.26	1.85	1.81	2.20	2.25	2.20
(Sm/Yb)	1.71	2.30	1.07	1.14	2.64	1.05	2.06	1.86	1.70	1.74	1.76	1.88	1.68
(Tb/Yb)n	1.15	1.73	1.15	0.85	1.59	1.22	1.43	1.49	1.05	1.15	1.52	1.45	1.49

n: Chondrite normalized (McDonough and Sun, 1995).

In the primitive mantle normalized spider diagram (Sun and McDonough, 1989) (Fig. 8B), the majority of samples are enriched in LILEs, such as Sr and Ba, and depleted in HFSEs, such as Nb and P, indicating the environment of island arcs (Al-Hamed et al., 2020). The spider diagram shows a positive Sr anomaly relative to neighboring elements due to its substitution for Ca in plagioclase. While Nb shows a negative anomaly, which reflects an island arc environment (Aswad et al., 2013). Moreover,

the spider diagram shows positive anomalies in Ba, K, and La in most samples, except that the troctolite sample shows a positive La anomaly due to early cumulate formation, with HREEs preferentially incorporated over LREEs (Rollinson, 1993).

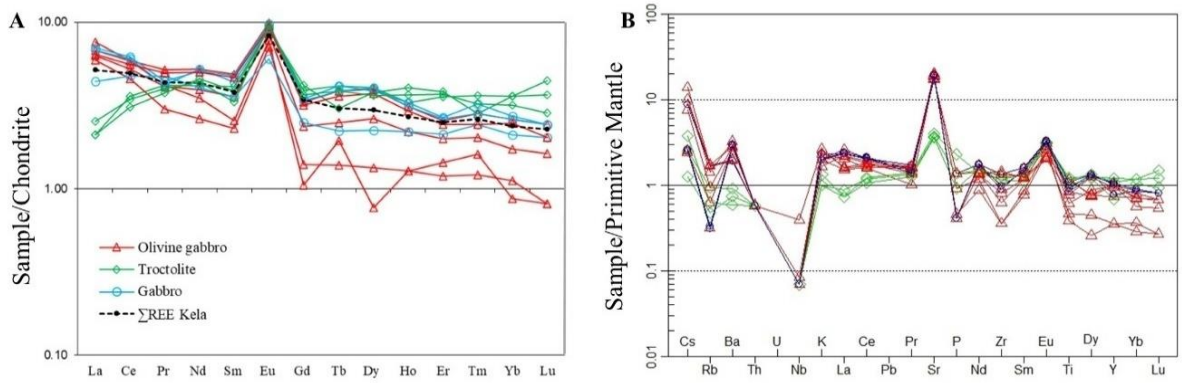

Fig.8. A) Chondrite normalized REE patterns (McDonough and Sun, 1995), and B) Primitive mantle spider diagram (Sun and McDonough, 1989)

4.5. Geothermobarometry

Several geothermobarometers were applied to determine the P-T condition of crystallization of the studied mafic rocks. Pyroxene chemistry is a powerful approach for estimating crystallization pressures and temperatures. Calibration by Brey and Köhler (1990) gives crystallization temperatures of 861-924˚C (average 894˚C). Two-pyroxene thermometry of Putirka (2008) gives temperatures of 882-938˚C (average 905˚C) and pressures of 5.1 to 8.6 kbar (average 6.7 Kbar) for pyroxene crystallization.

Ti in amphibole thermometry of Colombi (1989) indicates temperatures of 753-1016˚C (average 836˚C) for the studied mafic rocks. These calculated temperatures are in good agreement with results reported for the Wadi Rashid granitoid-gabbro suite, located approximately 30 km east of Qala Diza town, where kaersutite-based thermometry gives values of 933-935˚C (Aswad et al., 2013)

Ernst and Liu (1998) proposed an approach to indicate temperature and pressure by using TiO_2-Al_2O_3 isopleth from amphibole mineral compositions. In the amphibole minerals of the studied mafic rocks, TiO_2 range between 1.4-3.8 wt.% (average 2.2 wt.%) and Al_2O_3 between 11.0-13.3 wt.% (average 12.5 wt.%) (Table 5). These values yield a crystallization temperature of 750-940˚C (average 890˚C) and pressures 0.3 - 1.0 Gpa (average 0.65 Gpa) (i.e. 3-10 Kbar, average 6.5 Kbar) (Fig. 9).

The calculated pressures and temperatures conditions correspond to an approximate depth range of 19-21 km (Cloos, 1993).

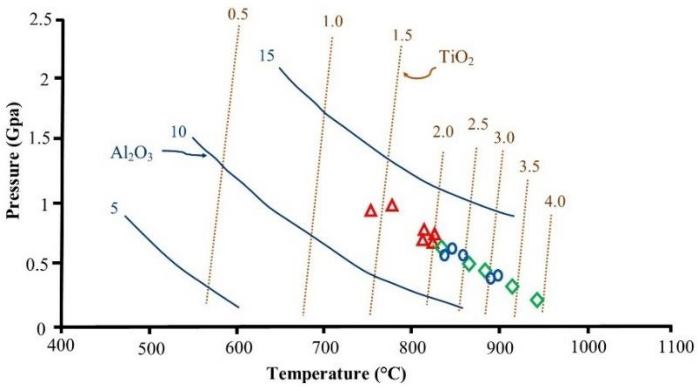

Fig.9. Al_2O_3 and TiO_2 isopleths (in wt.%) on P-T diagram of analyzed amphiboles (Ernst and Liu, 1998)

5. Discussion

The petrography examination identifies several igneous textures within the studied mafic rocks. The dominant textures observed are poikilitic, ophitic, sub-ophitic, and granular, which indicate slow cooling conditions of a mafic igneous body crystallizing at deep crustal levels within a subduction-related tectonic setting (Philpotts and Ague, 2009; Winter, 2014). Additionally, several less common textures were observed, such as corona texture, which indicates a solid-state reaction relationship between minerals (MacKenzie et al., 1982). Porphyroclastic texture, which indicates deformation due to tectonic forces resulting from tectonic stresses associated with thrusting during subduction (Winter, 2014). Exsolution texture, which indicates slow cooling below the solidus (Philpotts and Ague, 2009; Winter, 2014). and mesh texture, which indicates alteration or serpentinization of the olivine, a common alteration process in subduction zone's environments (MacKenzie et al., 1982).

The mineral chemistry of the studied mafic rocks (troctolite, olivine gabbro, and gabbro) reveals that plagioclase compositions in troctolite are bytownite, while in olivine gabbro and gabbro, they are labradorite. This compositional difference in plagioclase compositions may be related to the magmatic fractionation, revealing more sodic plagioclase with progressive magma differentiation (Leatherdale et al., 2003). This trend is consistent with the Anorthite–Albite binary solid-solution system, in which melts derived from plagioclase solid solutions are always more Na-rich than the solid, so progressive fractionation inevitably drives plagioclase compositions toward more sodic members (Winter, 2014). The clinopyroxene is classified as diopside, and the orthopyroxene as enstatite. Furthermore, the forsterite (Fo) content is highest in troctolite, followed by olivine gabbro, and the lowest in gabbro, providing additional evidence of crystal fractionation. The amphibole in the studied mafic rocks is predominantly secondary calcic amphibole, with compositions mainly corresponding to pargasite.

Geochemical analyses of major, trace, and rare earth elements were used to evaluate the petrogenesis of the studied mafic rocks. Two major processes are involved in the formation and evolution of the magma source: partial melting of the upper mantle peridotite and fractional crystallization. The (La/Sm)n vs. (Tb/Yb)n diagram (Wang et al., 2002) (Fig. 10A) and the (Sm/Yb)n vs. (La/Sm)n diagram (Lassiter and De Paolo, 1997) (Fig. 10B) suggest a spinel peridotite magma source for the studied mafic rocks. On Zr vs. Zr/Y diagram (Pearce and Norry, 1979) shows the majority of rock samples have partial melting of 15% (Fig. 10C).

The studied mafic rocks of the Bulfat Complex suggest the fractionation of early-forming minerals such as olivine, pyroxenes, amphibole, Ca-plagioclase, magnetite, and ilmenite during magmatic differentiation, as supported by a negative correlation between MgO and SiO_2 (Fig. 10D), and a positive correlation between MgO and Fe_2O_3 (Fig. 10E). The fractionation of Ca-plagioclase is associated with low K_2O and Na_2O contents, along with higher CaO and Al_2O_3 concentrations (Table 6). This fractionation is also indicated by the presence of a positive Eu anomaly in the studied mafic rocks (Fig. 8A). Fractionation of plagioclase and clinopyroxene is confirmed by trends observed in the Ti vs. Al_2O_3/TiO_2 diagram (Fig. 10F) as proposed by Pearce and Flower (1977).

The depletion in HFSE like Nb and P (Fig. 8B) is a characteristic feature of subduction-related magmas (Pearce, 1983), as these elements are generally immobile and remain within the subducted slab (Breeding et al., 2004). The enrichment of LILEs, like Sr and Ba (Fig. 8B) is attributed to their mobilisation by aqueous fluids, indicating the addition of slab-derived fluids to the mantle source (Breeding et al., 2004). Additionally, the negative anomalies in Nb and Zr (Fig. 8B), which are typical of volcanic arc magmas, are linked to the fractionation of these elements through the involvement of amphibole during dehydration and partial melting (Pearce, 1983). Moreover, positive anomalies in Sr, Ba, and K indicate an island arc setting associated with a subduction zone (Pearce, 1983; Wood, 1990; Al-Hamed et al., 2020).

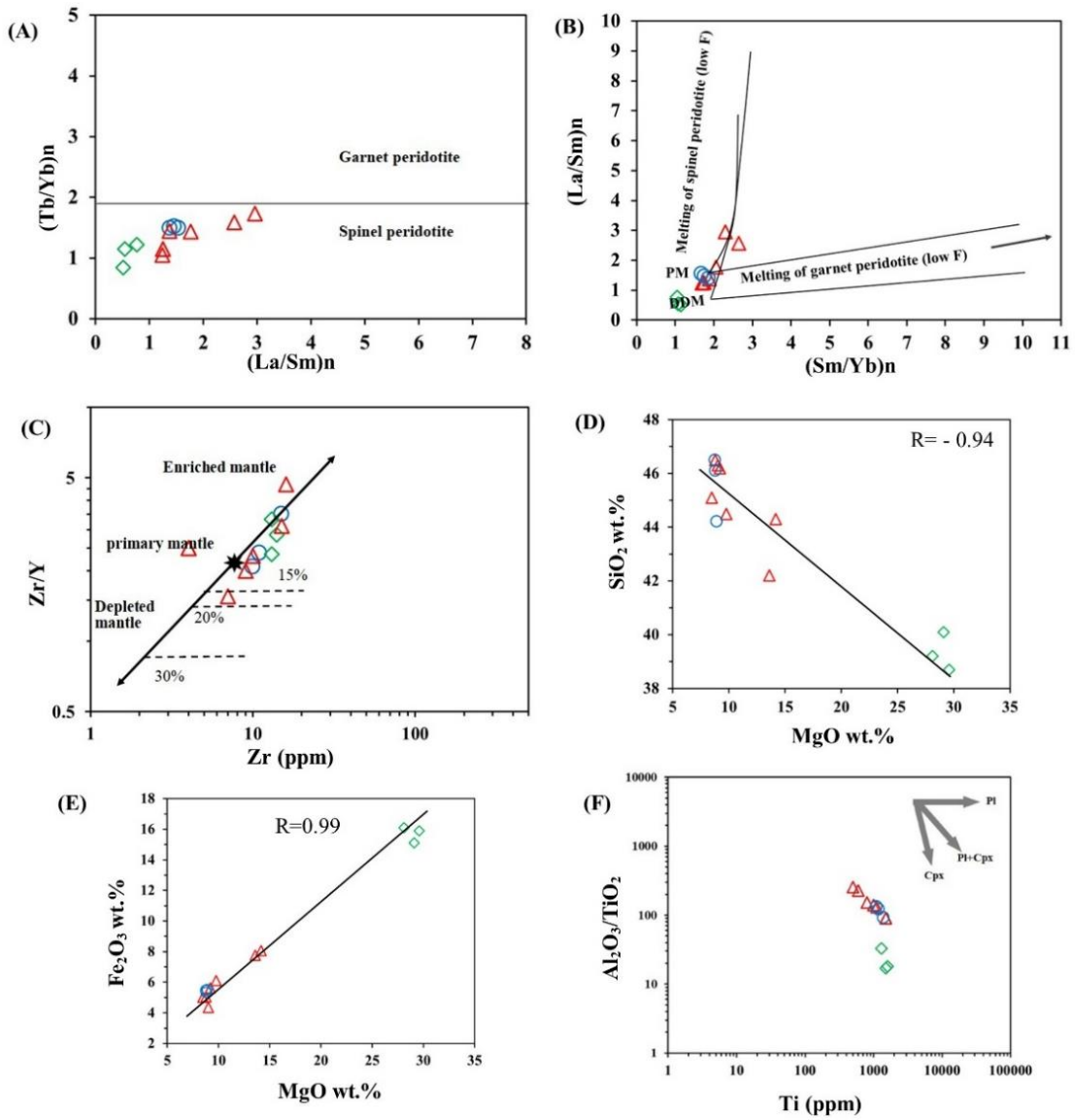

Fig. 10. Diagrams for the studied mafic rocks of the Bulfat Complex: A) (La/Sm)n versus (Tb/Yb)n diagram of after (Wang et al., 2002), B) (Sm/Yb)n vs. (La/Sm)n diagram after (Lassiter and De Paolo, 1997), C) Zr vs. Zr/Y diagram after (Pearce and Norry, 1979), D and E) Variation diagram of SiO_2 and Fe_2O_3 with MgO, and F) Ti versus Al2O3/TiO2 diagram (Pearce and Flower, 1977)

The tectonic geochemical discrimination diagrams, particularly the 2Nb-Zr/4-Y (Meschede, 1986; Fig. 11A) and Th-Hf/3-Nb/16 (Wood, 1980; Fig. 11B), indicate that the studied mafic rocks are primarily derived from a tectonic setting associated with a volcanic arc environment. A similar observation can be made from the MgO-FeO^t-Al_2O_3 diagram (Pearce et al., 1977) (Fig. 11C), where most of the studied mafic rocks fall within the volcanic arc basalt field. However, some samples were plotted within the MORB field, suggesting that these rocks formed in an extensional stress regime (Aswad et al., 2013). Notably, troctolite rocks fall outside the tectonic classification fields due to their high MgO content. The discrimination diagrams, Zr vs. Y (Müller et al., 2001) (Fig. 11D) confirm arc-related magma for the studied mafic rocks. Furthermore, the Nb/Yb vs. Th/Yb diagram (Pearce, 1983) (Fig. 11E), which is used to distinguish between volcanic arc basalts (VAB) and mid-ocean ridge basalts-ocean island basalts (MORB-OIB), emphasizes the volcanic arc field for the studied mafic rocks. Moreover, calculated pressures and temperatures of amphiboles in the studied mafic rocks (Fig. 9) are

another strong evidence for confirming the arc-related setting for the studied mafic rocks (Ernst and Liu, 1998; Müntener and Ulmer, 2018).

The geochemical evidence and tectonic discrimination diagrams indicate that the studied mafic rocks of the Bulfat Complex formed in subduction-related magmatism associated with the closure of the Neo-Tethyan Ocean. In a subduction-zone setting, partial melting of the mantle occurs and generates melts that ascend and undergo fractional crystallization; these processes ultimately produce mafic magmas. According to Cloos (1993), the calculated pressure (average 6.5 Kbar) corresponds to an approximate depth range between 19-21 km.

During the closure of the Neo-Tethyan Ocean, several magmatic activities occurred along the Zagros Suture Zone, leading to the formation of various ophiolites. This zone comprises two allochthons of arc-related rocks that have been obducted onto the Arabian Plate margin (Ali et al., 2012; Aswad et al., 2013). These two allochthons represent two different tectonic domains; the Upper Allochthon shows a proximal to Paleo-ridge intra-oceanic arc setting (Ali et al., 2019), whereas the Lower Allochthon is made of Walash and Naopurdan groups , characterized by a subduction-related tectonic setting with a melt component influenced by craton-derived sediments (Aswad, 1999).

The Bulfat Complex (~39 Ma) (Aswad et al., 2016) is located in the Upper Allochthon and intrudes the Albian-Cenomanian Gimo-Qandil sequence and ophiolite-bearing terrane (Jassim et al., 1982; Ali et al., 2012), while the Walash-Naopurdan arc Complex (32-43 Ma) is located in the underlying Lower Allochthon (Ali et al., 2012). Although these two allochthons are of approximately the same age, their distinct tectonic positions and geochemical signatures suggest they originated from two different subduction systems operating simultaneously in the Paleogene. This indicates the existence of two island arcs in the area, the first adjacent to the Arabian shelf and the second close to the middle of the paleo-ridge (Aswad et al., 2013, 2016).

The Neo-Tethyan Oceanic lithosphere is thought to have formed during the Albian-Cenomanian (97-118 Ma) (Aswad, 1999). This indicates that the Neo-Tethyan lithosphere was relatively old at the time of Paleogene subduction. Older and colder oceanic lithosphere generally subducts at a low angle because its higher density and lower buoyancy promote stronger mechanical coupling with the overriding plate, which in turn slows and resists slab descent (Isacks and Barazangi, 1997). This low-angle subduction is consistent with the density characteristics of the studied mafic rocks (average density 3.29 g/cm^3). This interpretation is also consistent with the studies of Khoshnaw et al. (2021) and Darin and Umhoefer (2022).

Cloos (1993), in his study on Lithospheric Buoyancy and Collisional Orogenesis, suggested that variations in crustal thickness and lithospheric buoyancy can obstruct subduction zones, alter plate motion and influence the style of convergence and orogeny. His analysis is fundamentally based on parameters derived from actual plate motions and the forces driving them. Cloos (1993) identified two types of subduction zones, warm and cold, based on their thermal structure, which is primarily controlled by the age of the descending plate, the speed of convergence, and the duration of subduction. The calculated P-T conditions of the studied mafic rocks suggest that they formed under a warm subduction zone, which is characterized by slow convergence speeds (e.g., < 2 cm/year) (Cloos, 1993; Seton et al., 2012; Matthews et al., 2016).

Global plate models by Seton et al. (2012) and Matthews et al. (2016) suggest that the relative plate motion of the Arabia and Africa plates relative to the Eurasia Plate changed over time, steadily decreasing from ~36 mm/year at 42 Ma to ~18 mm/year at 27 Ma. According to Cloos (1993), plate age (time) can be translated into distance when the convergence rate is known. Following this method, the Neo-Tethyan convergence distance can be calculated using the relation Distance = convergence rate x time interval, where the time interval corresponds to the duration between the onset of subduction and the onset of collision, considering that the onset of Paleogene subduction likely began around 45-44 Ma (Middle Eocene) (Ali et al., 2012; Aswad et al., 2016). Although the onset of collision between the

Arabia-Eurasian plates is debated, recent studies suggest that the collision began during the Late Oligocene to Early Miocene (Agard et al., 2005; Fakhari et al., 2008; Gavillot et al, 2010). Darin and Umhoefer (2022), in their study reconstructing the timing and location of the Arabia-Eurasian collision, placed the onset of collision in the central Zagros region (48° E) at ~27 Ma. At a convergence rate of ~18 mm/year, the total distance of the Neo-Tethyan Ocean during the Paleogene was approximately 324 km. This estimated distance is comparable to the value calculated by Koshnaw et al. (2021), who reported 283 ± 66 km at 40 Ma.

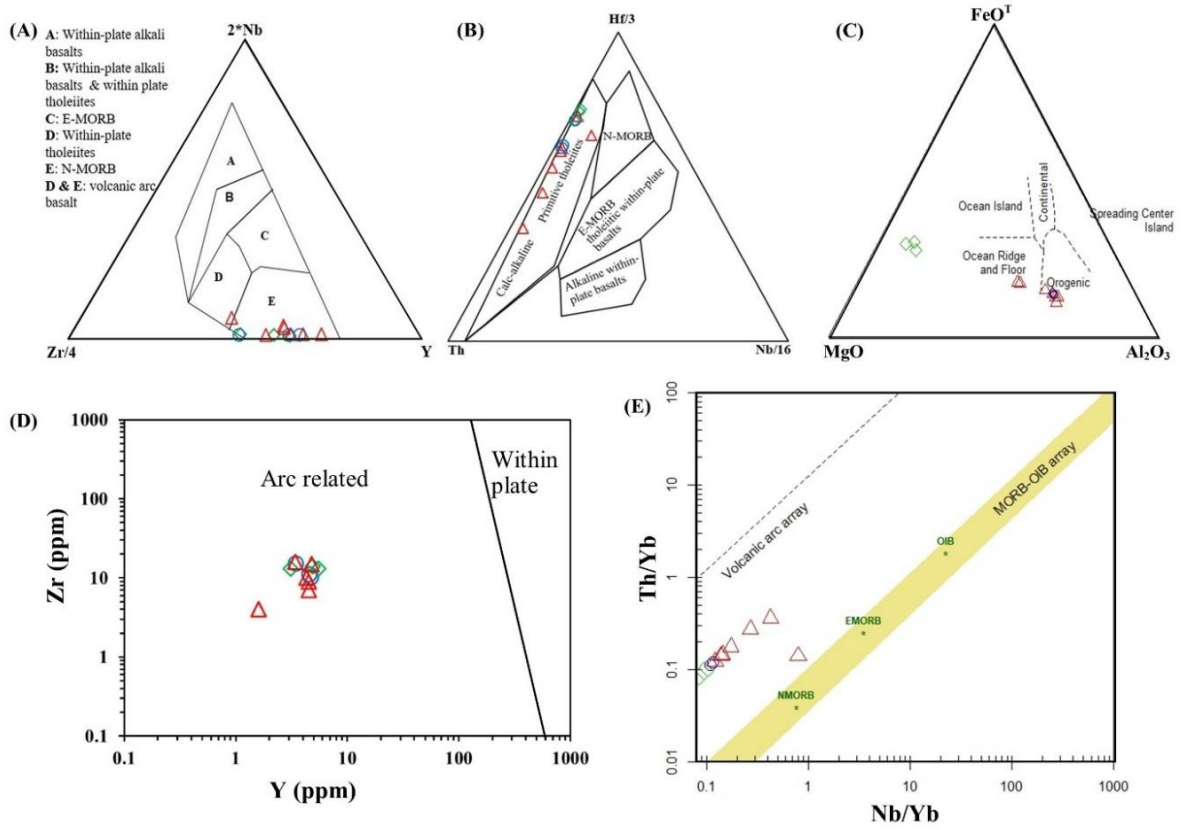

Fig.11. Tectonic classification diagrams of the Bulfat mafic rocks: A) The Nb-Zr-Y diagram (Meschede, 1986), B) The Th-Hf-Nb diagram (Wood, 1980), C) The MgO-FeOt- Al_2O_3 diagram (Pearce et al., 1977), D) The Zr vs. Y diagram (Muller et al., 2001), and E) The Nb/Yb vs. Th/Yb diagram (Pearce, 1983)

6. Conclusions

The petrogenesis and geochemical data of the studied mafic rocks of the Bulfat Complex provide clear evidence for their derivation from mantle-derived magmas that underwent fractional crystallization during emplacement. Field and petrographic observations revealed that plagioclase, pyroxene, and olivine are the dominant mineral phases, enabling the classification of the rocks as gabbro, olivine gabbro, and troctolite. These rocks exhibit a variety of igneous textures, including granular, ophitic, sub-ophitic, poikilitic, corona, porphyroclastic, exsolution, and mesh textures. The Electron Probe Micro Analysis (EPMA) revealed that plagioclase compositions range from bytownite to labradorite, clinopyroxene is diopside, and orthopyroxene is enstatite. The olivine falls within the chrysolite field, indicating that it is crystallized from magmas with a relatively primitive mantle source. The amphibole is predominantly secondary calcic amphibole, with compositions mainly corresponding to pargasite.

The whole-rock geochemistry indicates calc-alkaline to subalkaline affinity, low alkali and TiO_2 contents, and enriched LREE compared to HREE. The strong correlations between trace elements, such

as Ni and Co, with MgO (r=0.99 for both) reflect early crystallization from mantle-derived magmas. The relatively high Mg# values (69-75) indicate a more primitive mantle-derived magma. The enrichment in LILE, such as Sr and Ba and depletion in HFSE, such as Nb and P, alongside negative anomalies in Nb and positive anomalies in Sr, Ba, and K, collectively point to a magmatic origin in a subduction-related island arc environment. These features indicate that the studied mafic rocks originated from magma in a supra-subduction zone tectonic setting within the Zagros Suture Zone.

The geothermobarometric data of the studied mafic rocks of the Bulfat Complex record an average crystallization temperature of 890˚C and an average pressure of 6.5 Kbar, corresponding to a depth of 19-21 km, reflecting a warm subduction environment. These results suggest that the old Neo-Tethyan Ocean (Albian-Cenomanian) subducted at a low angle with a slow convergence rate (<2 cm/year). Based on this rate, the total distance of the Neo-Tethyan Ocean is estimated to be 324 km during Paleogene subduction.

References

Agard, P., Omrani, J., Jolivet, L., Mouthereau, F., 2005. Convergence history across Zagros (Iran): constraints from collisional and earlier deformation. International Journal of Earth Science, 94, 401-419. https://doi.org/10.1007/s00531-005-0481-4

Alavi, M., 1994. Tectonics of the Zagros orogenic belt of Iran: new data and interpretation. Tectonophysics, 229(3-4), 211-238. https://doi.org/10.1016/0040-1951(94)90030-2

Al-Hamed, S.T., Aswad, K.J., Aziz, N.R., 2019. Classification of Composite Pegmatite via Staining and Digital Image Processing in the Bulfat Complex, Qala Deza, NE (Iraq). In Conference of the Arabian Journal of Geosciences. Cham: Springer International Publishing, 291-298. https://doi.org/10.1007/978-3-030-01575-6_70

Al-Hamed, S.T., Aswad, K.J., Aziz, N.R., 2020. Geochemistry and petrogenesis of dioritic-gabbroic pegmatites in the Bulfat Complex, Qala Diza, Northeastern Iraq. Iraqi National Journal of Earth Sciences, 20(2), 64–90. 10.33899/earth.2020.170371

Ali, S.A., Nutman, A.P., Aswad, K.J., Jones, B.G., 2019. Overview of the tectonic evolution of the Iraqi Zagros thrust zone: Sixty million years of Neotethyan ocean subduction. Journal of Geodynamics, 129, 162–177. https://doi.org/10.1016/j.jog.2019.03.007

Aswad, K.J., 1999. Arc-continental collision in NE-Iraq as evidenced by the Mawat and Penjwin ophiolite complex. Rafedain Journal of Science, 10(1), 51–61.

Aswad, K.J., Sheraefya, R.M., Ali, S.A., 2013. Pre-collisional intrusive magmatism in the Bulfat Complex, Wadi Rashid, Qala Diza, NE Iraq: Geochemical and mineralogical constraints and implications for tectonic evolution of granitoid-gabbro suites. Iraqi National Journal of Earth Sciences, 13, 103–137.

Aswad, K.J., Ali, S.A., Sheraefy, R.M.A., Nutman, A.P., Buckman, S., Jones, B.G., Jourdan, F., 2016. $^{40}Ar/^{39}Ar$ hornblende and biotite geochronology of the Bulfat Igneous Complex, Zagros Suture Zone, NE Iraq: New insights on complexities of Paleogene arc magmatism during closure of the Neotethys Ocean. Lithos, 266, 406-413. https://doi.org/10.1016/j.lithos.2016.10.013.

Azizi, H., Moinevaziri, H., 2009. Review of the tectonic setting of Cretaceous to Quaternary volcanism in northwestern Iran. Journal of Geodynamics, 47(4), 167-179. https://doi.org/10.1016/j.jog.2008.12.002

Breeding, C.M., Ague, J.J., Bröcker, M., 2004. Fluid–metasedimentary rock interactions in subduction-zone mélange: implications for the chemical composition of arc magmas. Geology, 32(12), 1041-1044. https://doi.org/10.1130/G20877.1

BREY, G.P., Köhler, T., 1990. Geothermobarometry in four-phase lherzolites II. New thermobarometers, and practical assessment of existing thermobarometers. Journal of Petrology, 31(6), 1353-1378. https://doi.org/10.1093/petrology/31.6.1353

Buda, G., 1993. Igneous petrology of the Bulfat area (north-east Iraqi Zagros Thrust Zone). Acta Mineralogica Petrographica, 34, 21–39.

Buday, T., Jassim, S., 1987. The Regional Geology of Iraq: Tectonics, Magmatism, and Metamorphism. In: Kassab, I.I., Abbas, M.J., Eds., Geology of Iraq, Geologic Survey, Baghdad.

Cloos, M., 1993. Lithospheric buoyancy and collisional orogenesis: Subduction of oceanic plateaus, continental margins, island arcs, spreading ridges, and seamounts. Geological Society of America Bulletin, 105(6), 715–737. https://doi.org/10.1130/0016-7606(1993)105%3C0715:LBACOS%3E2.3.CO;2

Colombi, A., 1989. Metamorphism and geochemistry of mafic rocks from the central-western Alps (Viège-Domodossola-Locarno geoprofile). Mémoires de Géologie, 4. Lausanne: University of Lausanne, 1–216.

Darin, M.H., Umhoefer, P.J., 2022. Diachronous initiation of Arabia–Eurasia collision from eastern Anatolia to the southeastern Zagros Mountains since middle Eocene time. International Geology Review, 64(18), 2653–2681. https://doi.org/10.1080/00206814.2022.2048272

Deer, W.A., Howie, R.A., Zussman, J., 1992. An Introduction to the Rock-Forming Minerals (2nd ed.). Longman, Harlow. https://doi.org/10.1180/minmag.1992.056.385.20

Ernst, W.G., Liu, J., 1998. Experimental phase-equilibrium study of Al-and Ti-contents of calcic amphibole in MORB-A semiquantitative thermobarometer. American mineralogist, 83(9), 952-969. https://doi.org/10.2138/am-1998-9-1004

Fakhari, M.D., Axen, G.J., Horton, B.K., Hassanzadeh, J., Amini, A., 2008. Revised age of proximal deposits in the Zagros foreland basin and implications for Cenozoic evolution of the High Zagros. Tectonophysics, 451(1-4), 170-185. https://doi.org/10.1016/j.tecto.2007.11.064

Gavillot, Y., Axen, G.J., Stockli, D.F., Horton, B.K., Fakhari, M.D., 2010. Timing of thrust activity in the High Zagros fold-thrust belt, Iran, from (U-Th)/He thermochronometry. Tectonics, 29(4). https://doi.org/10.1029/2009TC002484

Irvine, T.H., Baragar, W.R.A., 1971. A guide to the chemical classification of the common volcanic rocks. Canadian journal of earth sciences, 8(5), 523-548. https://doi.org/10.1139/e71-055

Isacks, B.L., Barazangi, M., 1977. Geometry of Benioff zones: Lateral segmentation and downwards bending of the subducted lithosphere. Island Arcs, Deep Sea Trenches and Back-Arc Basins, 1, 99-114.

Jassim, S.Z., Buday, T., 2006. Tectonic Framework. In Goff, J.C., Jassim, S.Z., (Eds.), Geology of Iraq. Dolin, Prague; distributed by Geological Society of London.

Jassim, S.Z., Waldhausrova, J., Suk, M., 1982. Evolution of magmatic activity in Iraqi Zagros complexes. Krystalinikum, (16), 87-108.

Jassim, S.Z., Buday, T., Cicha, I., Opletal, M., Goff, J.C., 2006. Tectonostratigraphy of the Zagros suture. Geology of Iraq. Dolin, Prague and Moravian Museum, Brno, 199-211.

Jensen, L.S., 1976. A new cation plot for classifying subalkalic volcanic rocks. Ontario Division of Mines Miscellaneous Paper, 66.

Koshnaw, R.I., Schlunegger, F., Stockli, D.F., 2021. Detrital zircon provenance record of the Zagros mountain building from the Neotethys obduction to the Arabia–Eurasia collision, NW Zagros fold–thrust belt, Kurdistan region of Iraq. Solid Earth, 12(11), 2479-2501. doi:10.5194/se-12-2479-2021

Lassiter, J.C., DePaolo, D.J., 1997. Plume/lithosphere interaction in the generation of continental and oceanic flood basalts: chemical and isotopic constraints. Geophysical Monograph Series, 100, 335-355. https://doi.org/10.1029/GM100p0335

Le Bas, M. J., 1962. The role of aluminium in igneous clinopyroxenes with relation to their parentage. American Journal of Science, 260(4), 267-288. https://doi.org/10.2475/ajs.260.4.267

Leake, B.E., Woolley, A.R., Arps, C.E.S., Birch, W.D., Gilbert, M.C., Grice, J.D., Hawthorne, F.C., Kato, A., Kisch, H.J., Krivovichev, V.G., Linthout, K., Laird, J., Mandarino, J.A., Maresch, W.V., Nickel, E.H., Rock, N.M.S., Schumacher, J.C., Smith, D.C., Stephenson, N.C.N., Ungaretti, L., Whittaker, E.J.W., Youzhi, G., 1997. Nomenclature of amphiboles: Report of the Subcommittee on Amphiboles of the International Mineralogical Association, Commission on New Minerals and Mineral Names. American Mineralogist, 82(9–10), 1019–1037.

Leatherdale, S.M., Maxeiner, R.O., Ansdell, K.M., 2003. Petrography and geochemistry of the Love Lake leucogabbro, Swan River Complex, Peter Lake Domain, Northern Saskatchewan. Summary of Investigations, 2, 2003-4.

MacKenzie, W.S., Donaldson, C.H., Guilford, C., 1982. Atlas of igneous rocks and their textures (Vol. 148). Harlow: Longman.

Mason, B., Moore, C., 1982. Principles of Geochemistry. Wiley, New York.

Matthews, K.J., Maloney, K.T., Zahirovic, S., Williams, S.E., Seton, M., Müller, R.D., 2016. Global plate boundary evolution and kinematics since the Late Paleozoic. Global and Planetary Change, 146, 226-250. https://doi.org/10.1016/j.gloplacha.2016.10.002

McDonough, W.F., Sun, S.S., 1995. The composition of the Earth. Chemical Geology, 120(3–4), 223–253. https://doi.org/10.1016/0009-2541(94)00140-4

Meschede, M., 1986. A method of discriminating between different types of mid-ocean ridge basalts and continental tholeiites with the Nb-Zr-Y diagram. Chemical Geology, 56(3-4), 207-218. https://doi.org/10.1016/0009-2541(86)90004-5

Middlemost, E.A.K., 1994. Naming materials in the magma/igneous rock system. Earth-science reviews, 37(3–4), 215–244. https://doi.org/10.1016/0012-8252(94)90029-9

Moghadam, H.S., Stern, R.J., 2015. Ophiolites of Iran: Keys to understanding the tectonic evolution of SW Asia: (II) Mesozoic ophiolites. Journal of Asian Earth Sciences, 100, 31–59. https://doi.org/10.1016/j.jseaes.2014.12.016

Moghadam, H.S., Corfu, F., Stern, R.J., Lotfibakhsh, A., 2019. The Eastern Khoy metamorphic complex of NW Iran: a Jurassic ophiolite or continuation of the Sanandaj–Sirjan Zone?. Journal of the Geological Society, 176(3), 517–529. https://doi.org/10.1144/jgs2018-081

Morimoto, N., Fabries, J., Ferguson, A.K., Ginzburg, I.V., Ross, M., Seifert, F.A., Zussman, J., Aoki, K., Gottardi, G., 1988. Nomenclature of pyroxenes. American Mineralogist, 73(9–10), 1123–1133.

Müller, D., Franz, L., Herzig, P.M., Hunt, S., 2001. Potassic igneous rocks from the vicinity of epithermal gold mineralization, Lihir Island, Papua New Guinea. Lithos, 57(2-3), 163–186. https://dx.doi.org/10.1016/s0024-4937(01)00035-4

Müntener, O., Ulmer, P., 2018. Arc crust formation and differentiation constrained by experimental petrology. American Journal of Science, 318(1), 64-89. https://doi.org/10.2475/01.2018.04

Ottonello, G., Joron, J.L., Piccardo, G.B., 1984. Rare earth and 3d transition element geochemistry of peridotitic rocks:II. Ligurian peridotites and associated basalts. Journal of Petrology, 25(2), 373–403. https://doi.org/10.1093/petrology/25.2.373

Pearce, T.H., Gorman, B.E., Birkett, T.C., 1977. The relationship between major element chemistry and tectonic environment of basic and intermediate volcanic rocks. Earth and Planetary Science Letters, 36(1), 121–132. https://doi.org/10.1016/0012-821X(77)90193-5

Pearce, J.A., Flower, M.F.J., 1977. The relative importance of petrogenetic variables in magma genesis at accreting plate margins: a preliminary investigation. Journal of the Geological Society, 134(2), 103-127. https://doi.org/10.1144/gsjgs.134.2.0103

Pearce, J.A., Norry, M.J., 1979. Petrogenetic implications of Ti, Zr, Y, and Nb variations in volcanic rocks. Contributions to Mineralogy and Petrology, 69, 33–47. https://doi.org/10.1007/BF00375192

Pearce, J.A., 1983. Role of the sub-continental lithosphere in magma genesis at active continental margins. In: Hawkesworth, C.J., Norry, M.J., eds. Continental Basalts and Mantle Xenoliths. Nantwich: Shiva Publishing, 230–249. https://orca.cardiff.ac.uk/id/eprint/8626

Philpotts, A., Ague, J., 2009. Principles of Igneous and Metamorphic Petrology. 2nd ed. Cambridge: Cambridge University Press.

Poldervaart, A., 1950. Correlation of physical properties and chemical composition in the plagioclase, olivine, and orthopyroxene series. American Mineralogist: Journal of Earth and Planetary Materials, 35(11-12), 1067-1079.

Putirka, K.D., 2008. Thermometers and barometers for volcanic systems. Reviews in mineralogy and geochemistry, 69(1), 61–120. https://doi.org/10.2138/rmg.2008.69.3

Rollinson, H.R., 1993. Using Geochemical Data: Evaluation, Presentation, Interpretation. Longman, Harlow.

Seton, M., Müller, R.D., Zahirovic, S., Gaina, C., Torsvik, T., Shephard, G., Talsma, A., Gurnis, M., Turner, M., Maus, S., Chandler, M., 2012. Global continental and ocean basin reconstructions since 200 Ma. Earth-Science Reviews, 113(3–4), 212–270. https://doi.org/10.1016/j.earscirev.2012.03.002

Sissakian, V.K., Fouad, S.F., 2015. Geological map of Iraq, scale 1: 1000 000, 2012. Iraqi Bulletin of Geology and Mining, 11(1), 9-16.

Sofy, M.M., Aqrawi, A.M., 2007. Petrochemistry and Petrogenesis of Bulfat Mafic Intrusion, Qala Dizeh, Iraqi Kurdistan. Iraqi National Journal of Earth Science (INJES), 7(1), 33–0. https://doi.org/10.33899/earth.2007.39398

Streckeisen, A., 1974. Classification and nomenclature of plutonic rocks recommendations of the IUGS subcommission on the systematics of igneous rocks. Geologische Rundschau, 63(2), 773-786. https://doi.org/10.1007/BF01820841

Streckeisen, A.L., 1976. To each plutonic rock its proper name. Earth-science reviews, 12(1), 1–33. https://doi.org/10.1016/0012-8252(76)90052-0

Sun, S.S., McDonough, W.F., 1989. Chemical and isotopic systematics of oceanic basalts: implications for mantle composition and processes. Geological Society, London, Special Publications, 42(1), 313-345. doi: 10.1144/GSL.SP.1989.042.01.19

Trubelja, F., Marchig, V., Burgath, K.P., Vujović, Ž., 1995. Origin of the Jurassic Tethyan ophiolites in Bosnia: a geochemical approach to tectonic setting. Geologia Croatica, 48(1), 49-66. https://hrcak.srce.hr/18012

Wang, K., Plank, T., Walker, J.D., Smith, E.I., 2002. A mantle melting profile across the Basin and Range, SW USA. Journal of Geophysical Research: Solid Earth, 107(B1), ECV-5. https://doi.org/10.1029/2001JB000209

Winchell, A.N., 1951. Elements of optical mineralogy. Part II. Descriptions of minerals. Geologiska Föreningen i Stockholm Förhandlingar, 73(2), 319-320.

Winchester, J.A., Floyd, P.A., 1977. Geochemical discrimination of different magma series and their differentiation products using immobile elements. Chemical Geology, 20, 325-343. https://doi.org/10.1016/0009-2541(77)90057-2

Winter, J.D., 2014. Principles of Igneous and Metamorphic Petrology. 2nd ed. Pearson Education, Harlow.

Wood, D.A., 1980. The application of a Th-Hf-Ta diagram to problems of tectonomagmatic classification and to establishing the nature of crustal contamination of basaltic lavas of the British Tertiary Volcanic Province. Earth and Planetary Science Letters, 50(1), 11-30. https://doi.org/10.1016/0012-821X(80)90116-8

Wood, S.A., 1990. The aqueous geochemistry of the rare-earth elements and yttrium, Part 1: Review of available low-temperature data for inorganic complexes and the inorganic REE speciation of natural waters. Chemical Geology, 82, 159-186. https://doi.org/10.1016/0009-2541(90)90080-Q

Zrary, M.M.S., 2019. Petrogenesis and Geochemistry of Gabbro and Granitoid Plutonic Rocks in Bulfat Complex at Shakha Rash Mountain, Qala-Diza, NE- Iraq. PhD thesis, University of Mosul, Mosul.

Zrary, M.M., Aqrawi, A.M., Elias, E.M., 2022. Correction: Petrogenesis and tectonic setting of Shakha Rash granitoid, Bulfat intrusive complex, northeastern Iraq. Arabian Journal of Geosciences, 15(16), 1478. https://doi.org/10.1007/s12517-022-10760-9